



**PROVIDENCE WOMEN'S COLLEGE**

**COLLEGE WITH POTENTIAL FOR EXCELLENCE**

Re-Accredited with grade A<sup>+</sup> by NAAC

---

## **CRITERIA 3- RESEARCH INNOVATIONS AND EXTENSION**

### **Key Indicator 3.3- Research Publication and Awards**

**3.3.1: Number of research papers published per teacher in the journals notified on UGC care list during the last five years**



## Full Length Article

# Synergistic interaction of 2-amino 4-methyl benzothiazole (AMBT) and benzotriazole (BTZ) offers excellent protection to mild steel exposed in acid atmosphere at elevated temperatures: Electrochemical, computational and surface studies <sup>☆</sup>

K.M. Shainy, Anupama R. Prasad, Asha Thomas, Abraham Joseph <sup>\*</sup>

Department of Chemistry, University of Calicut, Calicut University P O, Kerala, India



## ARTICLE INFO

## Article history:

Received 10 July 2018

Revised 7 October 2018

Accepted 24 October 2018

Available online 14 January 2019

## Keywords:

Mild steel

AMBT

BTZ

Weight loss

EIS

Polarization

## ABSTRACT

The synergistic interactions and corrosion protection properties of 2-amino 4-methyl benzothiazole (AMBT) and 1, 2, 3-benzotriazole (BTZ) have been studied for mild steel in HCl at elevated temperatures. The extent of synergistic interaction increases with temperature. The methods of study include the conventional weight loss studies, computational screening, surface characterization and electrochemical studies. Quantum chemical approach was used to calculate some electronic properties of the molecules and to ascertain the synergistic interaction, inhibitive effect and molecular structures. The corrosion inhibition efficiencies and the global chemical reactivity relate to parameters like total energy,  $E_{\text{HOMO}}$ ,  $E_{\text{LUMO}}$  and gap energy ( $\Delta E$ ). Condensed atom Fukui functions also calculated using DFT at B3LYP/6-31G\* level, and were found to be correlating with the experimental results.

© 2019 Egyptian Petroleum Research Institute. Production and hosting by Elsevier B.V. This is an open access article under the CC BY-NC-ND license (<http://creativecommons.org/licenses/by-nc-nd/4.0/>).

## 1. Introduction

Organic molecules containing specific functional groups act as corrosion inhibitors for mild steel in different environments including industrial sectors [1]. Corrosion cannot be cured completely; instead the chemical process can be delayed to a reasonable time interval [1,2]. Acid pickling, acid de-scaling, oil-well acid in oil recovery, industrial cleaning, and petrochemical processes are some of the important applications of acid solutions in the industrial sectors. Aqueous acid solutions are powerful environments for metal deterioration especially when soluble products are formed. Among the prevention methods, development of suitable inhibitors and their strategic appropriation is the most investigated and relevant area of research [3,4]. The corrosion inhibitors can exhibit good adhesion property on metal surface and create a layer which shields the metal from aggressive environments [2]. In the past few decades this particular research stream is actively involved for the development of such inhibitors and their modified versions [3,4].

Organic molecules containing hetero atoms like S, N, and or O found to have greater inhibitive nature. The use of these molecules is one of the most practical approaches for the protection of metals and the efficiency depends on their adsorption ability on the metal surface by replacing water molecule in the metal/solution interface. The electron rich donor atoms trigger the active molecule to get adsorbed on the metal to offer passive action, or inhibition of electrode reactions. The effectiveness depends on the nature and surface charge of the metal, the corroding medium and the chemical structure of the inhibitor molecule [4,5]. Thus the compounds containing nitrogen, sulfur or oxygen and aromatic heterocyclic systems with conjugated double or triple bond structures have been widely used [5,6]. Combination of different inhibitors referred as synergistic interaction is of recent interest. Synergism is an adaptable strategy to develop safe and economically viable inhibitor combinations thereby increasing the performance, thermal resistance as well as reducing the inhibitor quantity [7]. The synergistic action of different organic inhibitor combinations in acidic aggressive media have been studied [5–6,8–11]. However, no reports exist in literature about the synergism between benzotriazole and thiazole systems like AMBT and BTZ for mild steel corrosion in hydrochloric acid.

Benzothiazole is a molecule with proven anticorrosion activity is used in the present study as part of the synergistic pair. The

Peer review under responsibility of Egyptian Petroleum Research Institute.

<sup>\*</sup> Corresponding author.E-mail address: [abrahamjoseph@uoc.ac.in](mailto:abrahamjoseph@uoc.ac.in) (A. Joseph).<https://doi.org/10.1016/j.ejpe.2018.10.002>

1110-0621/© 2019 Egyptian Petroleum Research Institute. Production and hosting by Elsevier B.V.

This is an open access article under the CC BY-NC-ND license (<http://creativecommons.org/licenses/by-nc-nd/4.0/>).

experiments have been conducted in the temperature range from 303 K to 323 K with an interval of 5 K. Methods like weight loss monitoring, electrochemical impedance spectroscopy and potentiodynamic polarization studies were employed. The surface monitoring of bare mild steel, inhibitor adsorbed and acid attacked specimens were carried out using SEM and AFM. Basic theoretical calculations were made using the DFT at the B3LYP/6-31G\* level using Gaussian 03 software. Parameters like ionization potential, electron affinity chemical reactivity and descriptors like hardness, softness and condensed atom Fukui function have been calculated.

## 2. Experimental

### 2.1. Materials and medium

Analytical grade reagents (97%) 2-amino-4-methyl benzothiazole and 1, 2, 3-benzotriazole were provided by Sigma Aldrich. The structure of BTZ and AMBT are given in Fig. 1. The mild steel sample of dimension  $2 \times 1.8 \text{ cm}^2$  was used for electrochemical studies and weight loss measurements. The samples contain the following composition of elements (weight by %): Fe (98.75%), C (0.2%), S (0.02%), P (0.03%) and Mn (1%). The samples were abraded using emery papers (400–1200 grade), and degreased by washing with acetone and then washed with distilled water [12]. Hydrochloric acid was provided by Merck. Anticorrosion studies were carried out in 0.5 M HCl at different temperatures.

### 2.2. Weight loss studies

The inhibition efficiency was determined using classical weight loss technique at room temperature. The pre-cleaned mild steel coupons were accurately weighed and immersed in the test solution with and without inhibitors for different time intervals. The reacted specimen taken out, cleaned, dried and weighed as recommended by ASTM. From the weight loss the corrosion rate and hence the inhibition efficiency were calculated.

### 2.3. Electrochemical measurements

A Gill AC computer controlled work station (ACM UK model no.1475) was used to carry out impedance spectra and potentiodynamic polarization measurements. The cell assembly consists of a platinum foil as the counter electrode, saturated calomel electrode coupled with fine Luggin capillary as the reference electrode and mild steel sample as the working electrode. All the electrode potentials were recorded with reference to the calomel electrode. 60 min was allowed to attain a stable value of electrode potential ( $E_{ocp}$ ) or equilibrium, prior to each measurement after the immersion of sample to the acid medium. The AC frequencies of  $10^{-1}$  Hz to  $10^{-4}$  Hz were applied for the excitation signal at amplitude of 10 mV. The polarization measurements were carried out in the potential range  $-250 \text{ mV}$  to  $+250 \text{ mV}$  with a sweep rate of

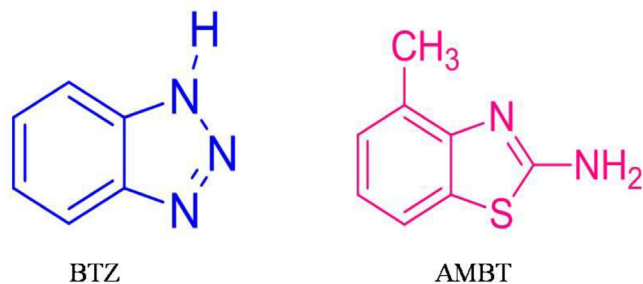


Fig. 1. Structure of inhibitors BTZ, AMBT.

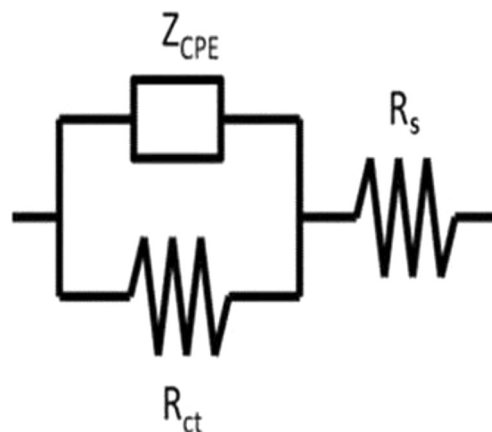


Fig. 2. Equivalent electrical circuit.

60 mV/min and the corresponding equivalent electrical circuit represented in Fig. 2. The electrode potential was determined by the extrapolation of linear Tafel regions through the corrosion potential  $E_{corr}$ . The corresponding current is obtained as the corrosion current density  $I_{corr}$ . The data processing was described as a non-linear least square method [13].

### 2.4. Surface characterization

The surface modifications of the metal sample in presence and absence of inhibitor/combination of inhibitors were monitored by using scanning electron microscope (SEM). The study was conducted using a Hitachi model SU 6600 scanning electron microscope. All micrographs were recorded at  $200\times$  magnification.

#### 2.4.1. Atomic force microscopy

The mild steel samples of  $2 \times 1.8 \text{ cm}^2$  were immersed in 0.5 M HCl in the absence and presence of the inhibitors in the individual and as a combination of BTZ-AMBT at 303 K for 4 h. The samples were then cleaned and dried to record the atomic force microscopic images.

### 2.5. Computational quantum chemical calculations

The geometries of BTZ, and AMBT were optimized at the B3LYP/6-31G\* level of DFT and frequency calculations at the same level of theory were done to confirm that the optimized structures are true minima on the potential energy surface. Parameters such as ionization potential (IP), electron affinity (EA), electronegativity (EN) hardness, softness and condensed to atom Fukui functions were evaluated by single point calculation at the same level of the theory [14–16]. The hydrogen bonding interaction between BTZ and AMBT was found out and optimized by the same software using the B3LYP/6-31G\* level of density functional theory. The frequency calculations were also done. The following theoretical relations between chemical parameters of molecules such as IP, EA, EN and hardness and the corresponding Frontier molecular orbitals had been well established in conceptual density functional theory [17].

$$E_{\text{HOMO}} = -\text{IP} \quad (1)$$

$$E_{\text{LUMO}} = -\text{EA} \quad (2)$$

$$-\mu = \frac{I + A}{2} = \chi \quad (3)$$

$$\eta = \frac{I - A}{2} \quad (4)$$

where  $\mu$  and  $\chi$  represent as Mulliken electro negativity and electronic chemical potential,  $\eta$  indicates chemical hardness. Eqs. (1) and (2) had been arrived at, based on the Koopmans theorem [18]. The fraction of electron transferred from the inhibitors to the metal surface was determined using the equation [19],

$$\Delta N = \frac{\chi_{\text{Fe}} - \chi_{\text{inh}}}{2(\eta_{\text{Fe}} - \eta_{\text{inh}})} \quad (5)$$

where  $\chi_{\text{Fe}}$  and  $\chi_{\text{inh}}$  is the absolute electronegativity of the metal (iron) and inhibitor molecules respectively.  $\eta_{\text{Fe}}$  and  $\eta_{\text{inh}}$  represent the absolute hardness of metal and inhibitors/combination.

The theoretical values of  $\chi_{\text{Fe}} = 7.0$  eV and  $\eta_{\text{Fe}} = 0$  were used for calculating the fraction of electrons transferred from inhibitor molecule to metal [19].

The evaluation of condensed Fukui functions is a better method for the measurement of reactivity, considering the finite difference approximation obtained from the Mulliken population analysis of atoms in the molecule. The electron density in the electrophilic and nucleophilic Fukui functions ( $f^+$  and  $f^-$ ) can be calculated using the finite difference approximation from Eqs. (6) and (7) [13],

$$f^+(r) = (\delta\rho(r)/\delta N)^+ v = q_{(N+1)}(r) - q_{(N)}(r) \quad (6)$$

$$f^-(r) = (\delta\rho(r)/\delta N)^- v = q_{(N)}(r) - q_{(N-1)}(r) \quad (7)$$

where  $\rho$ ,  $q(N+1)$ ,  $q(N-1)$  and  $q(N)$  are, the density of electrons, the NAO charges of the atom 'r', in the cationic, anionic, neutral systems of AMBT and BTZ and the combinations of inhibitors BTZ-AMBT.

### 3. Result and discussion

#### 3.1. Weight loss method and inhibition efficiency

The weight loss measurements were conducted by immersing mild steel samples in 0.5 M HCl. The difference in weight is recorded within the time intervals of 24, 48, 72 and 96 h. The inhibitors AMBT and BTZ were examined for their individual activity at their 200 ppm concentrations for each one in 0.5 M HCl. Anticorrosion studies of their synergistic pairs at a total concentration of 200 ppm in 0.5 M HCl was conducted. The degree of surface coverage ( $\theta$ ) was found out and the percentage inhibition efficiencies were calculated from the equation [15],

$$IE = \frac{W_0 - W}{W_0} \times 100 \quad (8)$$

where  $W_0$  and  $W$  are the weight loss of mild steel in the absence and presence of the inhibitors.

The weight loss data obtained for mild steel samples with various concentrations of AMBT and BTZ are represented in Table 1. The percentage inhibition efficiency corresponding to the selected time intervals are also mentioned in the Table. The results reveal

that mild steel corrosion rate was reduced on the addition of inhibitors in various combinations, and also in the individual form. Among all the combinations of BTZ-AMBT, 100 ppm BTZ (0.0008 M) and 100 ppm AMBT (0.0006 M) pairs exhibits the highest inhibition efficiency than the other combinations such as 50 ppm (0.0003 M) and 150 ppm (0.0012 M). The corrosion rate decreases with increase in immersion time. This may be due to the thickness of the adsorption layer which is uniform and compact at first thereafter suffer a gradual decay in uniformity with the increase in time of immersion 24 h–96 h.

#### 3.2. Impedance spectroscopic measurements (EIS)

EIS is a dependable tool for investigating the mechanism of anticorrosion activity of inhibitors on the metal-electrolyte interface especially when a protective layer is formed. It provides clear information on the resistive and capacitive behaviour of at the interface and to evaluate the performance of inhibitor/combination of inhibitors against the metal corrosion [20,21]. A combination of 50,100 and 150 ppm of AMBT and 150,100 and 50 ppm of BTZ were made to attain total of 200 ppm of BTZ-AMBT for each measurement. The impedance results were represented as Nyquist plots, in which the high frequency capacitive loop is linked to the charge transfer resistance ( $R_{ct}$ ). From the Nyquist plots it is clear that the synergistic pair which offers highest efficiency is 100 ppm–100 ppm of BTZ-AMBT and the plots are given in Fig. 3.

The increase in  $R_{ct}$ , leads to strong limitation of reduction of oxygen/the discharge of  $H^+$  ions, indicating strong inhibitive effect

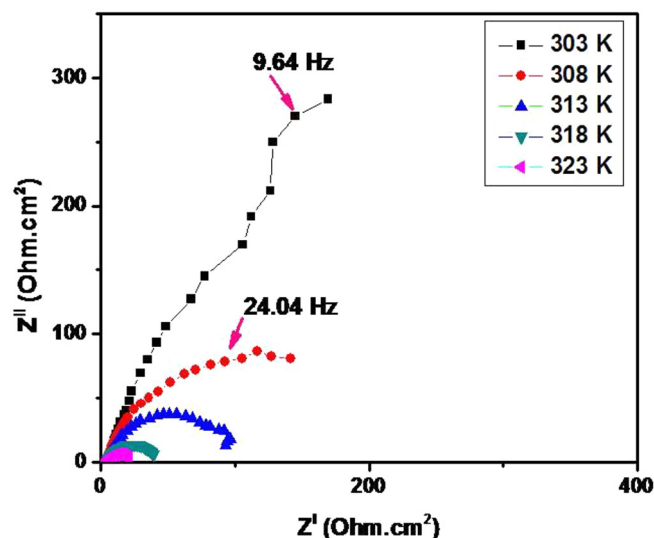


Fig. 3. EIS plots for mild steel in 0.5 M HCl in the presence 100 ppm BTZ –AMBT at different temperatures.

Table 1  
Percentage inhibition efficiency and weight loss data for AMBT - BTZ in 0.5 M HCl at 303 K.

AMBT-BTZ		% Inhibition Efficiency with time in hours and corresponding weight loss									
Inhibitor Concentration (ppm)											
AMBT	BTZ	Initial wt	Wt loss 24 h	% IE 24 h	Wt loss 48 h	% IE 48 h	Wt loss 72 h	% IE 72 h	Wt loss 96 h	% IE 96 h	
200	0	3.6671	0.7734	92.33	1.0611	90.14	1.0663	89.38	1.0686	86.12	
0	200	3.5773	0.0296	93.01	0.0412	92.52	0.0492	90.58	0.0512	90.34	
50	150	3.7366	0.0354	86.12	0.0461	85.47	0.0564	83.97	0.0584	83.69	
100	100	3.5292	0.0209	94.38	0.0346	93.82	0.0442	91.88	0.0460	90.87	
150	50	3.7375	0.0274	77.79	0.0403	75.13	0.1493	74.63	0.1522	73.26	

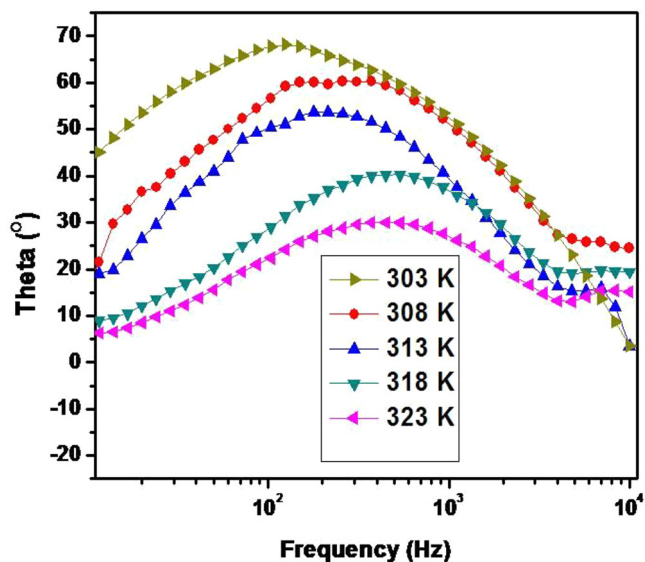


Fig. 4. Phase angle plots for mild steel in 0.5 M HCl in the presence 100 ppm BTZ - AMBT with temperatures.

of the synergistic pair. The adsorption relaxation or desorption is the reason for the low frequency inductive loop, indicating a negative change in the surface film on the metal [22,23]. For comparison, phase angle plots for the highest capacitive loop corresponding to 100 ppm of the pairs BTZ-AMBT at five different temperatures are given in Fig. 4.

The Nyquist plots are perfect semi-circle. The origin of depressed or suppressed semicircle observed in this case may be

due to the roughness or inhomogeneities of the electrode surface and the nature of current distribution [24]. From the capacitive loops for various concentrations of pairs of inhibitors, it is clear that the diameter of the loops is greater than zero concentration of inhibitors [25]. In fact the impedance of individual inhibitors increases to higher frequency at 303 K and decreases with temperatures. But the synergistic pair exhibit excellent inhibition even at higher temperatures. The percentage inhibition efficiency can be calculated from the charge transfer resistance of both inhibitors/pairs of inhibitors by the equation [15],

$$IE = \frac{R_{ct}^* - R_{ct}}{R_{ct}^*} \times 100 \quad (9)$$

where  $R_{ct}^*$  and  $R_{ct}$  are the charge transfer resistances in the presence and absence of inhibitors and their combinations respectively.

The EIS parameters such as  $R_{ct}$ ,  $C_{dl}$ , and  $IE\%$  for the corrosion of mild steel in HCl in the absence and presence of BTZ-AMBT are summarized in Table 2. Standard deviation for each concentration was calculated and mentioned in the same Table. It is clear from the Table that the value of double layer capacitance ( $C_{dl}$ ) decreases with increasing inhibitor concentration at 303 K. But at elevated temperatures the  $C_{dl}$  value is higher than that at 303 K. Normally rise in temperature causes the thickness of the inhibitor layer to decrease. Here the parallel relation of  $C_{dl}$  with temperature implies an increase in local dielectric constant or increase in the thickness of the double layer. The maximum efficiency is observed, when AMBT and BTZ are in equal concentration (100 ppm). The result shows that a stable adsorption film with more thermal resistance is formed on the surface of the metal by the addition of the inhibitor combinations.

The Bode modulus diagrams for the inhibitor pairs at five different temperatures are given in Fig. 5. From the figure the inhibition

Table 2  
EIS parameters for mild steel in the presence and absence of combination of AMBT-BTZ at different temperatures and standard deviation.

EIS parameters						
Temp.(K)	Concentration of BTZ	Concentration of AMBT	$R_{ct}$ ( $\Omega\text{cm}^2$ )	$C_{dl}$ ( $\mu\text{Fcm}^{-2}$ )	$IE\%$	Standard deviation
303	0	0	41.35	251.31	-	
	200	0	740.21	40.07	94.41	0.44
	0	200	840.33	38.63	95.07	0.78
	50	150	399.00	36.94	89.63	1.49
	100	100	651.90	40.35	93.65	1.17
	150	50	212.00	130.6	80.49	1.02
308	0	0	9.61	662.4	-	
	200	0	20.66	368.8	53.48	1.16
	0	200	45.66	190.6	78.95	1.14
	50	150	93.76	122.4	89.75	1.09
	100	100	215.70	84.31	95.54	0.97
	150	50	56.23	228.82	82.91	1.79
313	0	0	4.38	924.15	-	
	200	0	7.39	618.41	40.73	1.46
	0	200	48.43	132.2	89.16	1.64
	50	150	94.94	106.9	95.38	2.3
	100	100	200.3	73.5	97.81	1.27
	150	50	61.44	154.0	92.87	1.14
318	0	0	4.49	310.80	-	
	200	0	12.27	256.1	63.40	2.17
	0	200	14.02	166.1	67.97	1.73
	50	150	29.53	257.6	84.79	1.39
	100	100	37.80	130.7	88.12	1.01
	150	50	19.38	150.7	76.84	1.62
323	0	0	4.34	669.4	-	
	200	0	6.70	60.23	35.22	1.31
	0	200	7.52	888.1	42.28	1.26
	50	150	13.80	170.5	68.55	1.03
	100	100	16.64	22.09	73.91	1.00
	150	50	9.99	4.74	56.55	1.38

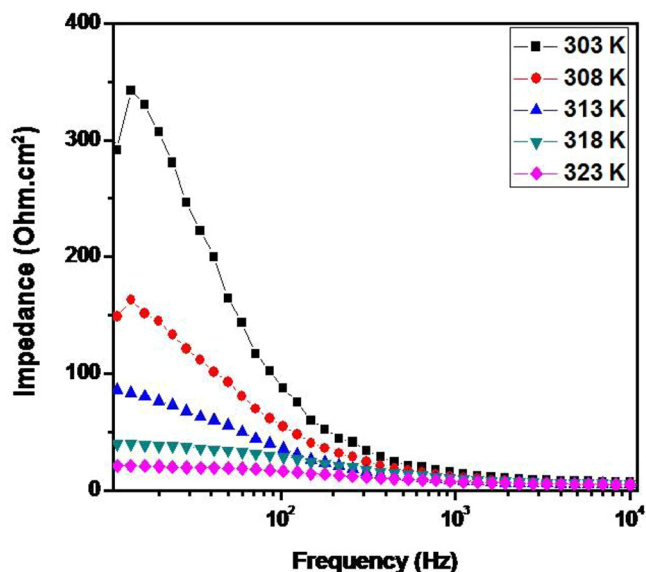


Fig. 5. Bode modulus plots for mild steel in 0.5 M HCl in the presence 100 ppm BTZ-AMBT with temperatures.

efficiency of low frequency impedance modulus for the combinations of inhibitors can be understood and this frequency increases with increasing concentration of inhibitors [26]. Therefore the adsorption of synergistic pair provides better corrosion resistance for mild steel in 0.5 M HCl and there is only one time constant corresponding to the formation of electrical double layer in the mild steel/HCl interface [26–28].

### 3.3. Tafel measurements

The Tafel polarization plot for mild steel in 0.5 M HCl at 303 K to 323 K in the absence and presence of inhibitors/combinations were measured. The Tafel plots for the synergistic pair of 100 ppm combinations of BTZ-AMBT (that shows highest polarization) are exhibited in Fig. 6 The percentage inhibition efficiency ( $IE\%$ ) was calculated using the equation [29],

$$IE = \frac{I_{\text{corr}} - I_{\text{corr}}^*}{I_{\text{corr}}} \times 100 \quad (10)$$

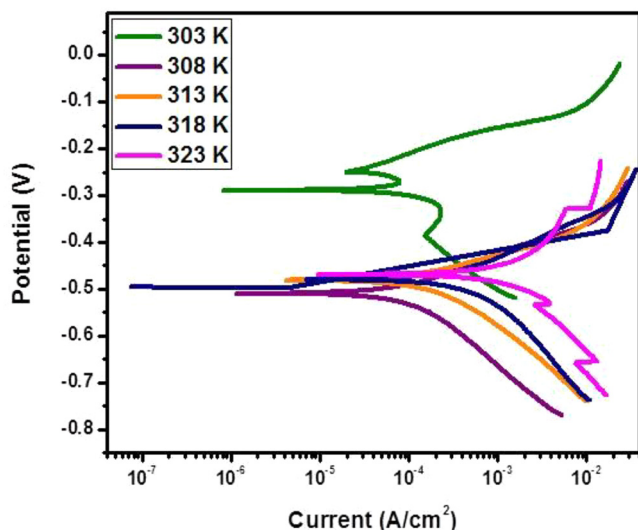


Fig. 6. Tafel plots for mild steel in 0.5 M HCl in the presence 100 ppm BTZ-AMBT at different temperatures.

where  $I_{\text{corr}}^*$  and  $I_{\text{corr}}$  are the corrosion current densities in the inhibited and uninhibited medium.

Polarization parameters such as  $I_{\text{corr}}$ ,  $E_{\text{corr}}$ , Tafel constants ( $\beta_a$  and  $\beta_c$ ) and  $IE\%$  for mild steel in the absence and presence of different combination of BTZ-AMBT are listed in Table 3. The inhibition efficiency of AMBT increases considerably in the presence of BTZ. The corrosion current densities in the presence of BTZ-AMBT remain comparatively low as compared to that in the uninhibited medium. The  $IE\%$  obtained for 100–100 ppm BTZ-AMBT was 82.14%, 91.17%, 96.15%, 87.75 and 69.29% corresponding to the temperature such as 303 K, 308 K, 313 K, 318 K, 323 K respectively. Moreover the corrosion potential is shifted towards more positive values in the presence of synergistic pairs. The displacement of  $E_{\text{corr}}$  with respect to the zero concentration determines the type of inhibition [29,30]. For AMBT-BTZ pair the displacement is within  $\pm 85$  mV which indicates a mixed inhibitive nature.

In acid solution the anodic reaction is the release of  $\text{Fe}^{2+}$  ions from the mild steel surface in to the HCl solution, and cathodic reaction is the discharge of  $\text{H}^+$  ions/reduction of oxygen in the acid medium. An inhibitor can affect either anodic/cathodic or both in some cases. In the present study the individual and the combined action of the inhibitors AMBT and BTZ, exhibit shift in both anodic and cathodic polarization behaviour, which in fact support mixed type behaviour of the inhibitor pair [28,31]. The addition 50,100 and 150 ppm of BTZ to azole system develop a strong adsorption and protective layer formation on the metal surface even at higher temperatures.

### 3.4. Effect of synergistic interactions of BTZ on AMBT

The individual performance of an inhibitor may be significantly improved by synergistic interactions. The improved inhibition efficiency due to synergistic action should be observed when the protonated species of the inhibitor is utilized. The synergism parameter was calculated from the equation [32],

$$S_0 = \frac{1 - \theta_1 - \theta_2 + (\theta_1\theta_2)}{(1 - \theta_{1+2})} \quad (11)$$

where  $\theta_1$  the surface coverage of BTZ,  $\theta_2$  is the surface coverage of AMBT.  $\theta_{1+2}$  are the surface coverage of BTZ-AMBT combinations. Generally,  $S_0 > 1$  indicates the synergistic effect whereas the values of  $S_0 < 1$  imply antagonistic behaviour of inhibitors [32,33].

The stabilization of the adsorbed layer of the inhibitor pair on the metal surface leads to greater surface coverage and hence greater inhibition. When temperature is raised, the efficiency got decreased, which may be attributed to the decomposition of inhibitor molecule at higher temperatures.

From Table 4, it is clear that the synergistic interaction significantly improves the inhibition efficiency of the inhibitor combinations. The synergistic parameters are almost higher than unity at higher temperatures. A pictorial representation of the synergistic interaction of BTZ-AMBT pair is shown in Fig. 7. There are two possibilities of hydrogen bonding interaction in the pair of BTZ-AMBT and hence establish a protective layer through a chemical force. At room temperature the individual system is dominating over inhibitor combinations, but  $IE\%$  increases with the rise in temperature (from 303 K to 313 K) due to the synergistic interaction. Therefore synergism is a good method for enhancing the inhibition efficiency of an inhibitor especially at higher temperatures.

It is evident from the calculated synergistic parameters that at higher temperatures  $S_0 > 1$ ; hence synergism is more favourable. This is due to adsorption of BTZ on the layer of AMBT. The values of  $S_0$  were found to decrease with an increasing inhibitor concentration. BTZ-AMBT-pair exhibits antagonistic behaviour at 303 K, which is evident from the  $S_0$  values ( $S_0 < 1$ ). Therefore cooperative

**Table 3**  
Polarization parameters for mild steel in the presence and absence of combination of AMBT-BTZ at different temperatures and percentage inhibition efficiency.

Temp. (K)	Inhibitor concentration		$\beta_a$ mV dec <sup>-1</sup>	$\beta_c$ (mV dec <sup>-1</sup> )	$-E_{corr}$ (mV)	$I_{corr}$ (mA cm <sup>-2</sup> )	$IE\%$
	BTZ	AMBT					
303	Zero concentration		67.92	-92.60	274.15	0.28	-
	200	0	42.35	-43.95	259.14	0.0082	97.07
	0	200	63.52	-76.84	447.84	0.015	94.64
	50	150	46.48	-56.61	237.34	0.02	92.85
	100	100	48.47	-94.44	278.09	0.05	82.14
	150	50	50.44	-59.84	266.28	0.08	71.42
308	Zero concentration		42.70	37.41	472.77	0.34	-
	200	0	51.46	-53.32	498.17	0.09	73.52
	0	200	33.58	-36.45	470.81	0.15	55.88
	50	150	31.56	-35.86	481.5	0.06	82.35
	100	100	44.43	-54.17	509.99	0.03	91.17
	150	50	34.78	-31.45	483.34	0.07	79.41
313	Zero concentration		87.23	-95.73	475.24	1.04	-
	200	0	55.77	-53.74	500.05	0.12	88.46
	0	200	63.19	-98.14	477.47	0.68	34.61
	50	150	49.05	-62.37	492.93	0.06	94.23
	100	100	46.78	-58.13	508.39	0.04	96.15
	150	50	43.50	-45.79	492.93	0.07	93.26
318	Zero concentration		84.21	-149.69	456.44	0.49	-
	200	0	31.09	-39.84	485.26	0.14	71.42
	0	200	42.58	-38.51	457.81	0.13	73.46
	50	150	22.66	-26.84	477.02	0.07	85.71
	100	100	21.95	-23.20	478.44	0.06	87.75
	150	50	26.93	-29.01	485.32	0.12	75.51
323	Zero concentration		152.98	-200.01	502.11	1.14	-
	200	0	24.65	-36.97	458.85	0.69	39.47
	0	200	71.81	-146.47	453.21	0.77	32.45
	50	100	49.49	-38.88	469.59	0.40	64.91
	100	100	53.42	-49.72	492.49	0.35	69.29
	150	50	80.24	-79.74	491.73	0.47	58.77

**Table 4**  
Synergistic interactions of BTZ- AMBT on mild steel at different temperatures.

Inhibitor combination	Concentration of BTZ	Concentration of AMBT	Synergistic Parameters ( $S_0$ )					
			Weight loss method(303 K)	Electrochemical method				
				303 K	308 K	313 K	318 K	323 K
BTZ - AMBT	50	150	0.4142	0.5273	0.3459	9.0594	1.4219	1.2409
	100	100	0.3500	0.2060	0.6650	2.7380	2.3273	1.7333
	150	50	0.0791	0.1306	0.1964	2.1572	1.6800	1.2788

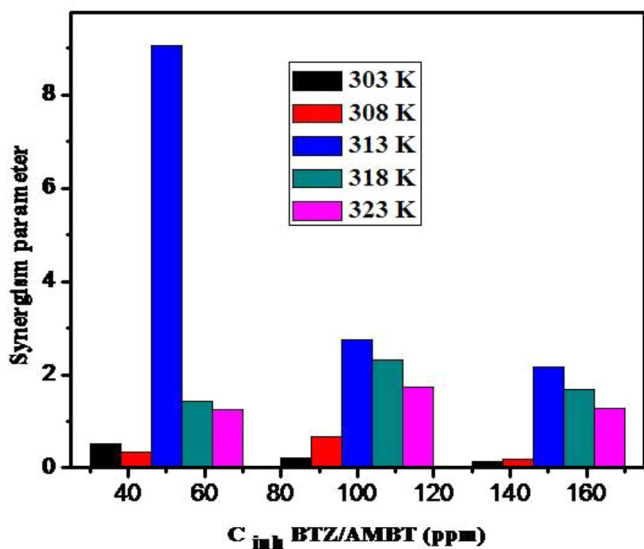


**Fig. 7.** Variation of synergistic parameter at different temperature in the presence of BTZ -AMBT.

adsorption is expected for BTZ-AMBT pair. The order of synergistic reactivity of BTZ-AMBT at various temperatures follows 323 K > 318 K > 313 K > 308 K > 303 K.

There is no synergistic behaviour on 303 K instead noticed an antagonistic behaviour. From 308 K onwards the inhibitor combinations show a synergistic interaction, which is evident from the increase in inhibition efficiency of the combined form compared to the individual performance. The synergistic interaction shows its maximum efficiency at 313 K and on further increase of temperature, the synergistic interaction is noticed at a lesser extent.

### 3.5. Adsorption studies

Molecular structures of the inhibitors/combination of inhibitors play an important role in adsorption interactions. Hence the adsorption of the inhibitor on the mild steel surface explains the formation of direct bonding between the hetero atoms and vacant d-orbital of Fe atoms present on the mild steel surface.

Adsorption isotherms were examined to study the synergistic corrosion inhibition of BTZ-AMBT pair for mild steel in 0.5 M HCl at three different temperatures. Various adsorption isotherms were

tested, Langmuir adsorption isotherm was the best description, and is represented by the equation [34],

$$\frac{C_{inh}}{\theta} = C_{inh} + \frac{1}{K_{ads}} \quad (12)$$

where  $C_{inh}$  is the concentration of inhibitor and  $K_{ads}$  is the equilibrium constant. The standard free energy of adsorption [34],

$$\Delta G^\circ = -RT \ln (55.5K_{ads}) \quad (13)$$

where the constant 55.5 is the molar concentration of water and  $R$  is the universal gas constant.  $T$  is the absolute temperature in Kelvin. According to the Langmuir equation the expected plots of  $C/\theta$  versus  $C_{inh}$  is a straight line with a slope and regression coefficient approximately equal to 1 at different temperatures [34–40] and the plots are given in Fig. 8.

The negative free energy of adsorption  $\Delta G^\circ$ , provides insight in to the nature of the adsorption process on working electrode with synergistic pairs. In general the free energy of adsorption,  $\Delta G^\circ$  up to  $-20$  kJ/mol indicates a weak interaction, hence electrostatic in nature (physisorption). When the values are close to  $-40$  kJ/mol

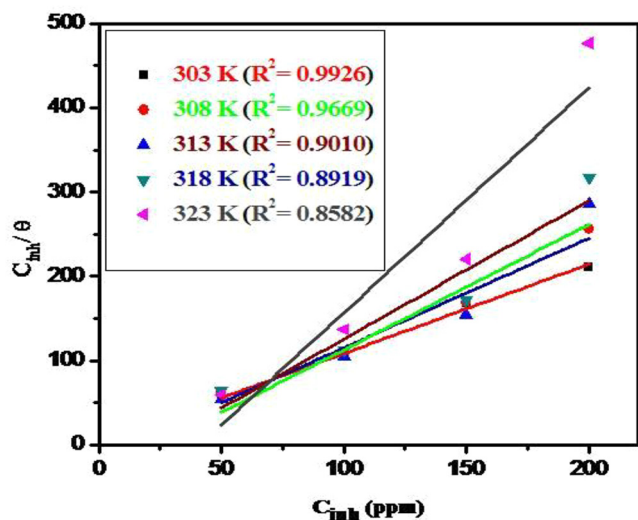


Fig. 8. Langmuir adsorption isotherm plots for mild steel in 0.5 M HCl in the presence of BTZ-AMBT.

Table 5

Thermodynamic parameters for BTZ-AMBT for corrosion of mild steel corrosion at various temperatures and concentrations.

Inhibitor combination	Temp.(K)	Inhibitor concentration					
		50–150		100–100		150–50	
		$\Delta G_{ads}^\circ$ (kJ/mol)	$K_{ads}$ (L/mol)	$\Delta G_{ads}^\circ$ (kJ/mol)	$K_{ads}$ (L/mol)	$\Delta G_{ads}^\circ$ (kJ/mol)	$K_{ads}$ (L/mol)
BTZ-AMBT	303	-37.16	45711.35	-36.66	37572.72	-32.44	70971.93
	308	-36.26	32015.06	-36.66	37572.72	-32.31	6689.54
	313	-37.72	57124.21	-37.56	53733.03	-33.91	12626.99
	318	-38.74	41431.07	-37.17	22855.67	-33.91	6689.54
	323	-36.02	12005.64	-36.66	15275.16	-31.69	2401.37

Table 6

Corrosion kinetic parameters for mild steel in 0.5 M HCl solution in the absence and presence of various concentrations of BTZ-AMBT.

Inhibitor combination	Inhibitor concentration	$E_a$ (kJ/mol)	$\Delta H^\circ$ (kJ/mol)	$\Delta S^\circ$ (J K <sup>-1</sup> mol <sup>-1</sup> )
BTZ-AMBT	Zero concentration	121.1400	218.5397	219.8873
	50–150	174.4951	171.8934	60.4147
	100–100	258.0690	155.4682	3.8629
	150–50	132.2000	129.6043	2.6204

or more negative, it suggests the sharing/transfer of electrons from the synergistic pair to the mild steel surface to form a relatively strong bonding (chemisorption) [41,42]. Inhibitors in the present investigation shows a free energy of adsorption  $-33$  to  $-40$  kJ/mol hence there is a possibility of physical and chemical adsorption (Table 5).

Thermodynamic parameters determine the spontaneity of adsorption. Gibbs-Helmoltz and Van't Hoff equations were helpful for calculating thermodynamic parameters such as entropy ( $\Delta S_{ads}^\circ$ ) and enthalpy of adsorption ( $\Delta H_{ads}^\circ$ ). The negative sign of  $\Delta S_{ads}^\circ$  and  $\Delta H_{ads}^\circ$  indicates the exothermic behaviour of the adsorption of process. The evolution of less heat accompanied by the weak interaction whereas more heat evolution is accompanied by strong interaction such as chemisorptions. The reduction in entropy can be due to the ordered arrangement of organic inhibitors from aqueous solution to a solid metal surface [43].

### 3.6. Kinetic aspects of the corrosion process

The calculation of corrosion kinetic parameters reveals the influence of temperature on the corrosion process of mild steel in 0.5 M HCl in the absence and presence of BTZ-AMBT pair. The study has been conducted in the temperature range of 303 K–323 K. The free energy of adsorption,  $\Delta G_{ads}^\circ$  and  $K_{ads}$  obtained are summarized in Table 5. The enthalpy of activation ( $\Delta H^\circ$ ), entropy of activation ( $\Delta S^\circ$ ) and activation energy ( $E_a$ ) were also calculated from the Arrhenius equation and transition state equation [44–47].

$$\ln CR = \frac{-E_a}{RT} + \ln A \quad (14)$$

$$\ln \frac{CR}{T} = \ln \frac{R}{nh} + \frac{\Delta S^\circ}{R} + \frac{\Delta H^\circ}{RT} \quad (15)$$

where  $CR$  is the rate of corrosion,  $A$  is the pre-exponential factor,  $T$  is the temperature in Kelvin,  $h$  is the Planks constant,  $R$  is the universal gas constant and  $N$  is the Avogadro number.

A plot of  $CR/T$  versus  $1/T$  gives a straight line, the intercept and slope of which provides the values for  $\Delta H^\circ$  and  $\Delta S^\circ$ . The plot of  $\ln CR$  versus  $1/T$  gives a straight line and its slope gives  $E_a$ . Literature explicitly reveals that an increase in  $E_a$  value in the presence of the inhibitor indicates physisorption and any trend in the opposite direction may be an indication of deviation from physisorption to chemisorptions [45–47]. The synergistic

interaction between BTZ-AMBT combinations shows a declining trend in  $E_a$  values with increasing concentration. The corrosion kinetic parameters in the absence and presence of various concentrations of BTZ-AMBT were noted in Table 6. This may be attributed to the strong chemisorption of the inhibitor pair on the metal surface. This is further evident from the  $\Delta G_{ads}^{\circ}$  values obtained for the various combinations of inhibitor pairs. The values of  $\Delta H^{\circ}$  also show similar trend.  $\Delta S^{\circ}$  increases at first and then decreases with increasing concentration of BTZ and AMBT in the reaction medium.

A similar trend of increase in entropy and  $E_a$  is obtained in the presence of inhibitors than uninhibited solution. If the activation energy is higher in the presence of an inhibitor, indicates the weak interaction between the metal and aggressive medium. In the pre-

sent report, it is evident that  $E_a$  decreases as the concentration of BTZ-AMBT increases. The decrease in entropy is associated with an increase in adsorption of inhibitors. From the Table it is clear that the entropy decrease as adsorption increases [48,49].

### 3.7. Molecular electronic properties of inhibitor system

DFT calculations have proven to be an excellent support in the interpretation of theoretical and experimental results. The experimental results suggest that the inhibition efficiency of synergistic pair is greater than that of individual molecules. These findings could be fully rationalized by the theoretical parameters calculated using the B3LYP/6-31G\* level of Density Functional Theory. The optimized geometry,  $E_{HOMO}$ ,  $E_{LUMO}$  and  $E_{LUMO}-E_{HOMO}$  gap for the

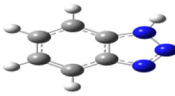
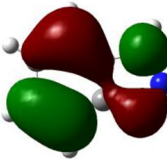
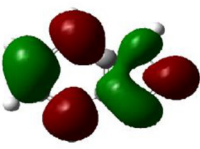
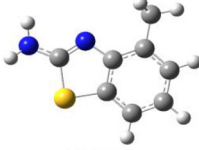
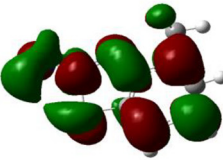
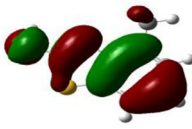
Optimized structure of inhibitors	HOMO	LUMO	Theoretical Parameters
 BTZ			TE = -395.8671 $E_{HOMO}$ = -6.5551 $E_{LUMO}$ = -1.1973 $\Delta E$ = 5.3578
 AMBT			TE = -817.3804 $E_{HOMO}$ = -5.6544 $E_{LUMO}$ = -0.3129 $\Delta E$ = 5.3415

Fig. 9. Optimized geometry and HOMO and LUMO of BTZ, AMBT and theoretical parameters.

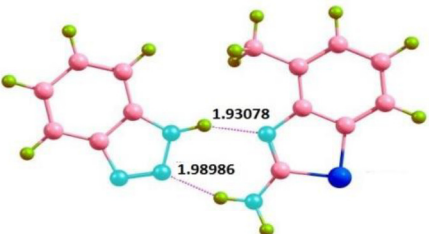
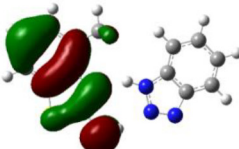
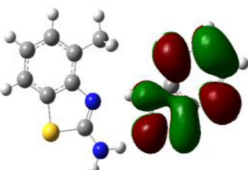
Synergistic interactions	HOMO	LUMO	Theoretical Parameters
 BTZ-AMBT			E = -1213.041 $E_{HOMO}$ = -5.7524 $E_{LUMO}$ = -1.1347 $\Delta E$ = 4.6177

Fig. 10. Synergistic interactions and theoretical parameters of BTZ -AMBT.

Table 7

Chemical reactivity descriptors for the inhibitors and their combination BTZ, AMBT, and BTZ – AMBT pair.

Inhibitors	Chemical reactivity descriptors						
	IP(eV)	EA(eV)	$\chi$ (eV)	$\eta$ (eV)	$\mu$ (D)	$\sigma$	$\Delta N$
BTZ	6.5551	1.1973	3.8762	2.6789	4.0038	0.3734	0.5830
AMBT	5.6544	0.3129	2.9837	2.6708	1.8812	0.3744	0.7519
BTZ-AMBT	5.7524	1.1347	3.4436	2.3089	2.0288	0.4331	0.7701

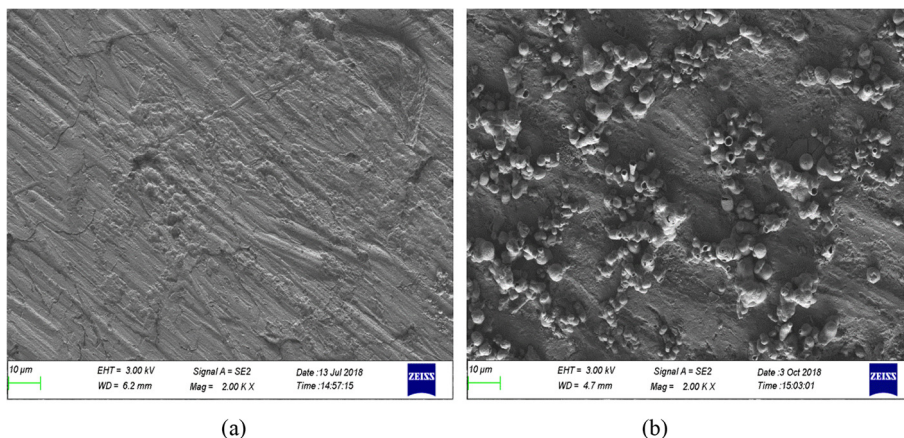
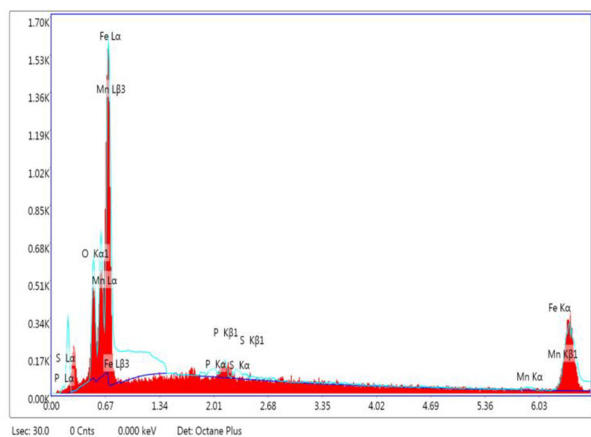
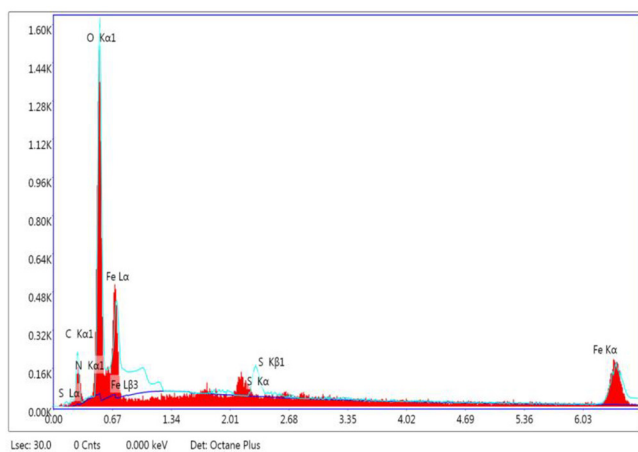


Fig. 11. SEM images of (a) Zero concentration of synergistic pair, (b) presence of BTZ-AMBT.

individual systems (AMBT/BTZ) are consolidated in Fig. 9. Higher  $E_{HOMO}$  of the inhibitor leads to higher ability of electron donation and higher inhibition efficiency is indicated by the smaller value of  $\Delta E$ . H- Bonding interaction of AMBT-BTZ pairs and theoretical parameters ( $E_{HOMO}$ ,  $E_{LUMO}$ ,  $\Delta E$  etc.) are represented in Fig. 10. From the Figure, the higher  $E_{HOMO}$  value for the combined form indicates



(a)



(b)

Fig. 12. (a) EDS image and mapping of mild steel in the absence AMBT-BTZ, (b) EDS image and mapping of mild steel containing BTZ-AMBT.

a greater possibility of donating electrons to the vacant d-orbital of Fe and the lower  $E_{LUMO}$  value suggest the capability to receive electrons from the metal surface easily [50,51]. The value of  $\Delta E$  for the synergistic pair BTZ-AMBT is 4.6177 eV. The chemical descriptors such as hardness, softness, dipole moment are also given in Table 7. The dipole moment of the synergistic pair BTZ-AMBT was 2.0288D which is a measure of the polarity of a polar covalent bond. The total dipole moment reflects the global polarity of a molecule. Moreover high dipole moment will enhance the inhibition efficiency to high value due to the increased dipole-dipole interaction between the inhibitor molecules and the metal surface [52,53]. The fraction of electrons transferred to the metal surface by AMBT-BTZ pair is  $\Delta N = 0.7701$ , proving its higher inhibition efficiency compared to individual members. Lower value of  $E_{LUMO}-E_{HOMO}$  gap of this pair strongly supports the above findings. The chemical hardness (used to compare the intermolecular reactivity) value of the synergistic pair AMBT-BTZ is 2.3089.

The reactivity descriptor for the region selectivity in a nucleophilic/electrophilic reaction may be determined in the study of less common reaction mechanism involving more exotic reactants (the influence of BTZ) as a function of Fukui calculation. The reactivity of the synergistic pairs BTZ-AMBT was investigated using the Fukui function  $f^+$  or  $f^-$  at the B3LYP/6-31G\* level of Density Functional Theory, which gives a correct explanation of intermolecular reactivity of the sequence of atoms in the synergistic pair [54]. The atoms in which the possibility of electrophilic and nucleophilic attack is designated as maximum value of  $f^+$  or  $f^-$ . The Fukui indices for the individual systems are exhibited in (Table S1 and S2 (supplementary data)). From these Tables the reactivity orders of individual inhibitors are computed to be BTZ > AMBT. Table S2, given in Supplementary Data indicates that the synergistic pairs have a most favourable electrophilic and nucleophilic centres to interact with the metal surface.

### 3.8. Surface morphological studies

Surface morphology of mild steel specimen with and without inhibitors was carried out by Scanning Electron Microscopy. Fig. 11(a) shows the uninhibited mild steel specimen in 0.5 M HCl after the immersion of 4 h. The observed number of cracks on the surface of metal due to the direct attack of acid. Fig. 11(b) shows the image of mild steel specimen immersed in HCl containing 100–100 ppm concentration of BTZ-AMBT which is a smooth surface. The introduction of BTZ and AMBT in to the 0.5 M acid has reduced the corrosion rate which is evident from the considerable decrease in surface heterogeneity. Thus the metal corrosion is

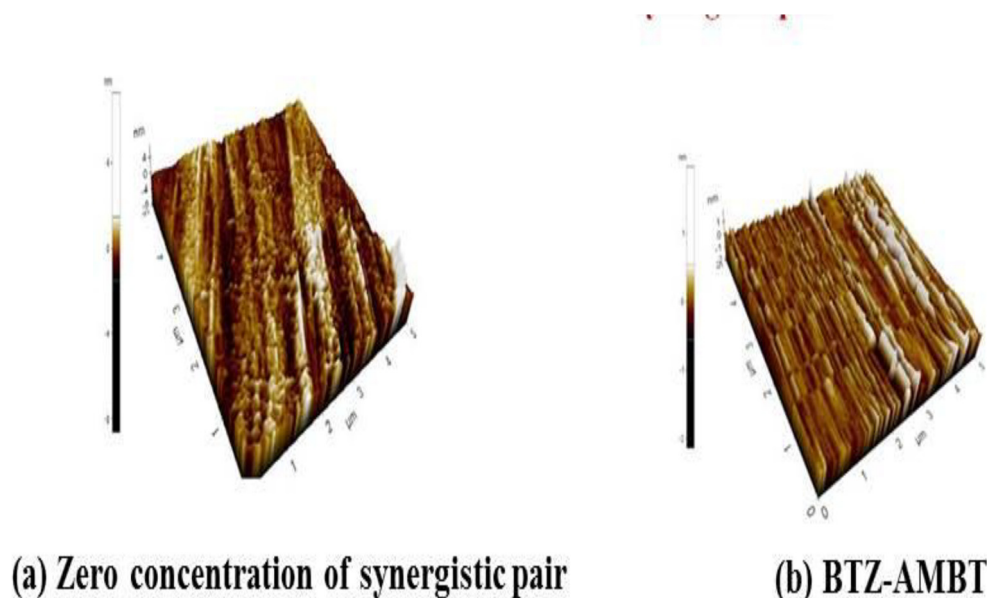


Fig. 13. AFM images of metal specimen in the absence and presence of BTZ –AMBT pair.

prevented by the deposition of BTZ and AMBT on the metal surface. The results of EDS analysis of sample exposed in acid in the presence of BTZ and AMBT is presented in Fig. 12. An inspection of elements and their percentage on metal surface in the presence of the inhibitors further support the adsorption and the formation of protective layer of the inhibitor pair. The EDS image of bare mild steel sample has the following elemental percentage 85.83% Fe, 9.41% Oxygen, 0.51% Phosphorous, 3.87% Manganese and 0.38% Sulphur (Fig. 12(a)), whereas that of the inhibited sample is 36.62% Fe, 11.28 Carbon, 47.96% Oxygen, and 0.21% nitrogen, 3.93% sulphur which indicates the formation of a protective layer of BTZ and AMBT with the on the surface (Fig. 12(b)).

Atomic force microscopy has become a better method to evaluate the action of inhibitors on the metal/solution interface [55–57]. The 3D images of the mild steel specimen in the absence and presence of the inhibitor/synergistic pairs at 303 K are shown in Fig. 13 (a & b). In the absence of inhibitors the metal surface is highly damaged due to the direct attack of ionic species present in HCl and the corresponding image is given in the same Figure. The roughness of the mild steel specimen for uninhibited reaction medium was noted as 0.547 nm. It can be observed that after the addition of inhibitor to the corrosive medium, significant differences are visible on the surface morphology of the mild steel specimen. The average roughness of the surface of mild steel specimen recorded in the presence of BTZ-AMBT pair is estimated to be 0.230 nm. The result reveals that the corrosion rate get decreased to higher extent by the addition of BTZ–AMBT pair due to the effective adsorption of this pair on mild steel surface

#### 4. Conclusions

The synergistic action of BTZ- AMBTpair provides excellent inhibition of mild steel corrosion in 0.5 M HCl.

1. As revealed from SEM micrographs the mild steel surface is undamaged, smooth and crack free after the addition of BTZ-AMBT pair due to the formation of a protective monolayer on the surface.
2. The adsorption process follow Langmuir adsorption isotherm model.

3. The strong synergistic interaction between AMBT and BTZ decreases its further ability to form stable adsorption layer. Therefore co adsorption may be expected for better synergistic inhibition efficiency for BTZ-AMBT at 313 K, 318 K and 323 K.
4. The observed roughness parameters indicate that BTZ –AMBT is a better synergistic pair on higher temperature.
5. Comparison of theoretical data generated using B3LYP/6–31G\* level of Density Functional Theory and experimental values have better correlation, proving the reliability of the quantum mechanical techniques in the study of the synergistic interaction of BTZ-AMBT on mild steel. The reactivity descriptors such as hardness ( $\eta$ ), softness ( $\sigma$ ), electronegativity ( $\mu$ ), fraction of electron transferred ( $\Delta N$ ) and Fukui indices further confirm the inhibition efficiency of BTZ- AMBT pair.

#### Appendix A. Supplementary data

Supplementary data to this article can be found online at <https://doi.org/10.1016/j.ejpe.2018.10.002>.

#### References

- [1] G. Trabaneli, *Corrosion* 47 (1991) 410–419.
- [2] H. Ashassi-Sorkhabi, B. Shaabani, D. Seifzadeh, *Appl. Surf. Sci.* 239 (2005) 154–164.
- [3] H. Ashassi-Sorkhabi, M. Es'haghi, *Mater. Chem. Phys.* 114 (2009) 267–271.
- [4] F. Bentiss, M. Lebrini, M. Lagrenee, *Corros. Sci.* 47 (2005) 2915–2931.
- [5] S.K. Shukla, M.A. Quraishi, *Corros. Sci.* 51 (2009) 1990–1997.
- [6] S. Issaadi, T. Douadi, A. Zouaoui, S. Chafaa, M.A. Khan, G. Bouet, *Corros. Sci.* 53 (2011) 1484–1488.
- [7] F. Bentiss, M. Bouanis, B. Mernari, M. Trasnel, M. Lagrenee, *J. Appl. Electrochem.* 32 (2002) 671–678.
- [8] X.H. Zhang, Q.Q. Liao, K.B. Nie, L.L. Zhao, D. Yang, Z.W. Yue, H.H. Ge, Y.J. Li, *Corros. Sci.* 93 (2015) 201–210.
- [9] D. Ben Hmamouti, R. Salghi, A. Zarrouk, B. Hammouti, S.S. Al-Deyab, Lh. Bazzi, H. Zarrok, A. Chakir, L. Bammou, *Int. J. Electrochem. Sci.* 7 (2012) 2361–2373.
- [10] M. Bouklah, N. Benchat, A. Aouniti, B. Hammouti, M. Benkaddour, M. Lagrenee, H. Vezin, F. Bentiss, *Prog. Org. Coat.* 51 (2004) 118–124.
- [11] K.F. Khaled, *Corros. Sci.* 52 (2010) 3225–3234.
- [12] ASTM G-31-72, Standard recommended practice for the laboratory immersion corrosion testing of metals, in: *Annual Book of ASTM standard*, ASTM International, West Conshohocken, P.A., 1990, p. 401.
- [13] Sam John, Abraham Joseph, *RSC Adv.* 2 (2012) 9944–9951.
- [14] N.O. Eddy, Part 3, *Mol. Simul.* 36 (2010) 354–363.

- [15] K.F. Khaled, *Electrochim. Acta* 55 (2010) 6523–6532.
- [16] E.E.E. Benso, D.A. Isabirye, N.O. Eddy, *Int. J. Mol. Sci.* 11 (2010) 2473–2498.
- [17] T. Anup, K. Bhanuprakash, *Chem. Phys. Chem.* 13 (2012) 597–605.
- [18] R.G. Parr, W. Yang, *J. Am. Chem. Soc.* 106 (1984) 4049–4050.
- [19] Z. El Adnani, M. Mcharfi, M. Sfaira, M. Benzakour, A.T. Benjelloun, M. Ebn Touhami, *Corros. Sci.* 68 (2013) 223–230.
- [20] Bingru Zhang, Chengjun He, Cheng Wang, Peidi Sun, Fengting Li, Yu. Lin, *Corros. Sci.* 94 (2015) 6–20.
- [21] Songqing Hua, Ailing Guo, Yufeng Genga, Xiaolin Jia, Shuangqing Suna, Jun Zhang, *Mater. Chem. Phys.* 134 (2012) 54–60.
- [22] D.A. Lopez, S.N. Simison, S.R. de Sanchez, *Electrochim. Acta* 48 (2003) 845–854.
- [23] S.A. Umoren, Y. Li, F.H. Wang, *Corros. Sci.* 52 (2010) 2422–2429.
- [24] A. Popova, S. Raicheva, E. Sokolova, M. Christov, *Langmuir* 12 (1996) 2083–2089.
- [25] B.P. Markhali, R. Naderi, M. Mahdavian, M. Sayebani, S.Y. Arman, *Corros. Sci.* 75 (2013) 269–279.
- [26] M.A. Hegazy, A.M. Badawi, S.S.A.E. Rehim, W.M. Kamel, *Corros. Sci.* 69 (2013) 110–122.
- [27] M. Motamedi, A.R. Tehrani-Bagha, M. Mahdavian, *Corros. Sci.* 70 (2013) 46–54.
- [28] Yongming Tang, Fan Zhang, Hu. Shengxiang, Ziyi Cao, Wu. Zhenglei, *Wenheng jing, Corros. Sci.* 74 (2013) 271–282.
- [29] K.F. Khaled, S.S. Abdel-Rehim, G.B. Sakir, *Arab. J. Chem.* 5 (2012) 213–218.
- [30] E.S. Ferreira, C. Giancomelli, A. Spinelli, *Mater. Chem. Phys.* 83 (2004) 129–134.
- [31] Xu. Bin, Wenzhong Yang, Ying Liu, Xiaoshuang Yin, Weinan Gong, Yizhong Chen, *Corros. Sci.* 78 (2014) 260–268.
- [32] H. Tavakoli, T. Shahrabi, M.G. Hosseini, *Mater. Chem. Phys.* 109 (2008) 281–286.
- [33] Ahmed A. Farag, M.A. Hegazy, *Corros. Sci.* 74 (2013) 168–177.
- [34] Yuanming Ren, Jing Zhang, Du. Min, Longwei Niu, *Res. Chem. Intermed.* 42 (2016) 641–657.
- [35] M.K. Pavithra, T.V. Venkatesha, K. Vathsala, K.O. Nayana, *Corros. Sci.* 52 (2010) 3811–3819.
- [36] I.B. Obot, N.O. Obi-Egbedi, S.A. Umoren, *Corros. Sci.* 51 (2009) 276–282.
- [37] K. Ramya, Revathi Mohan, Abraham Joseph, J. Taiwan Inst. Chem. Eng. 1015 (2014) 12–23.
- [38] A. Kosari, M.H. Moayed, A. Davoodi, R. Parvizi, M. Momeni, H. Eshghi, H. Moradi, *Corros. Sci.* 78 (2014) 138–150.
- [39] M.A. Hegazy, M. Abdallah, H. Ahmed, *Corros. Sci.* 52 (2010) 2897–2904.
- [40] Wen Chen, Hongqun Luo, Nianbing Li, *Corros. Sci.* 53 (2011) 3356–3365.
- [41] Ahmed Y. Musa, Amir H. Abdul, Kadhum., Abu Bakar Mohamad, Mohd Sobri Takriff, Abdul Razak Daud, Siti Kartom Kamarudin, *Corros. Sci.* 52 (2010) 526–533.
- [42] V. Ramesh Saliyan, A.V. Adhikari, *Corros. Sci.* 50 (2008) 55–61.
- [43] A.S. Fouda, K. Shalabi, G.Y. Elewady, H.F. Merayyed, *Int. J. Electrochem. Sci.* 9 (2014) 7038–7058.
- [44] Ahmed Y. Musa, Abu Bakar Mohamad, Amir H. Abdul, Kadhum, Mohd Sobri Takriff, Lim Tien Tien, *Corros. Sci.* 53 (2011) 3672–3677.
- [45] Dileep Kumar Yadav, M.A. Quraishi, B. Maiti, *Corros. Sci.* 55 (2012) 254–266.
- [46] Ashish Kumar Singh, M.A. Quraishi, *Corros. Sci.* 52 (2010) 1529–1535.
- [47] Xingwen Zheng, Shengtao Zhang, Wenpo Li, Linliang Yin, Jiahong He, Wu. Jinfang, *Corros. Sci.* 80 (2014) 383–392.
- [48] Xianghong Li, Shuduan Deng, Xiaoguang Xie, Fu. Hui, *Corros. Sci.* 87 (2014) 15–26.
- [49] X.H. Li, S.D. Deng, G.N. Mu, H. Fu, F.Z. Yang, *Corros. Sci.* 50 (2008) 420–430.
- [50] Xianghong Li, Xiaoguang Xie, J. Taiwan. Inst. Chem. Eng. 45 (2014) 3033–3045.
- [51] G. Gao, C. Liang, *Electrochim. Acta* 52 (2007) 4554–4559.
- [52] N. Soltani, M. Behpour, E.E. Oguzie, M. Mahluji, M.A. Ghasemzadeh, *RSC Adv.* 5 (2015) 11145–11162.
- [53] Lukman O. Olasunkanmi, Ime B. Obot, Mwadham M. Kabanda, Eno E. Ebenso, *J. Phys. Chem. C* 119 (2015) 16004–16019.
- [54] P. Geerlings, F. De Proft, W. Langenaeker, *Chem. Rev.* 103 (2003) 1793–1873.
- [55] Xiumei Wang, Huaiyu Yang, Fuhui Wang, *Corros. Sci.* 55 (2012) 145–152.
- [56] Ali Doner, Ramazan Solmaz, Muzaffer Ozcan, Gulfeza Kardas, *Corros. Sci.* 53 (2011) 2902–2913.
- [57] Sudhish Kumar Shukla, M.A. Quraishi, Cefalexin drug, *Mater. Chem. Phys.* 120 (2010) 142–147.

Eur. Phys. J. A (2019) **55**: 73

DOI 10.1140/epja/i2019-12745-y

## $\rho$ -meson spectral function in hot asymmetric nuclear matter

P.C. Raje Bhageerathi



Società  
Italiana  
di Fisica



Springer

# $\rho$ -meson spectral function in hot asymmetric nuclear matter

P.C. Raje Bhageerathi<sup>a</sup>

Department of Physics, Providence Women's College, Calicut-673009, Kerala, India

Received: 3 October 2018 / Revised: 30 January 2019

Published online: 20 May 2019

© Società Italiana di Fisica / Springer-Verlag GmbH Germany, part of Springer Nature, 2019

Communicated by R. Rapp

**Abstract.** The  $\rho$ -meson spectral function in hot and dense asymmetric nuclear matter (number densities of proton and neutron different) is evaluated in an effective chiral  $SU(3)$  model within the mean field approximation (MFA). The dependence of the vector meson masses on density and temperature, their variation with the asymmetry parameter, the form of the spectral function when the  $p \longleftrightarrow n$  symmetry is broken are studied. One can observe a clear splitting of the longitudinal and the transverse modes among the  $\rho$  isospin multiplets. The role of a running tensor coupling on the spectral function is also studied.

## 1 Introduction

The behaviour of vector mesons in nuclear matter under extreme conditions has attracted a lot of attention during the recent years, both theoretically and experimentally. The properties of hadrons at high temperatures and densities are quite different from the properties of hadrons in vacuum. The medium modification of hadrons has direct consequences on the experimental observables from the strongly interacting matter produced in heavy ion collision experiments. The reduction of the vector meson masses in hot and/or dense nuclear matter could be regarded as a possible signal of the restoration of chiral symmetry [1, 2]. The study of the  $\rho$  meson in the medium is particularly interesting, because of the fact that it can decay directly to lepton pairs [3, 4].

The in-medium properties of the vector mesons have been extensively studied within the framework of different models [5–7]. Since different formalisms lead to different results, there exists a lot of controversy regarding these issues. The Brown and Rho [1] scaling suggests a dropping of the vector meson masses in the medium. Gale and Kapusta [8] have earlier analyzed the modification of the  $\rho$  meson self-energy at finite temperature in an isospin-symmetric pion medium. They have observed the medium corrections to be modest even upto a temperature of about 0.15 GeV. Chin [9] in his pioneering work predicted an increase in the mass of the  $\omega$  meson in the dense nuclear matter within the mean field approximation (MFA), where the contribution from the Dirac sea ( $n - \bar{n}$  pair production) is not considered. The mass of the  $\omega$  meson has been found to decrease in dense nuclear

matter by Jean *et al.* [10] by taking into account of both the Fermi and the Dirac sea effects. Within the framework of QHD-I and chiral  $SU(3)$  models, it is reported that the peak of the spectral function shifts towards lower invariant mass regions in RHA, while it is centered around the nominal  $\rho$ -pole in MFA [11] in isospin symmetric medium. The work by Gale and Kapusta has been extended to an isospin-asymmetric pion medium with large values of the charge chemical potential  $\mu$  [12]. They have predicted an asymmetry in the emission rate of the dileptons. The effect of the asymmetry parameter on the masses of the  $\rho^0$ ,  $\rho^+$  and the  $\rho^-$ -mesons is studied in [13], where it has been shown that the  $\rho^+$ -meson takes slightly higher and the  $\rho^-$ -meson takes slightly lower masses compared to the  $\rho^0$ , with increasing values of the nucleon density. The propagation of the light mesons  $\sigma$ ,  $\omega$ ,  $\rho$ , and  $a_0(980)$  in dense hadronic matter is investigated in an effective relativistic hadronic model inspired in the derivative scalar coupling model (DCM) [14].

In this paper, we attempt to study the properties of the  $\rho$  meson by considering its propagation in hot and dense asymmetric nuclear matter focussing on the role of  $p \longleftrightarrow n$  symmetry breaking using an effective Lagrangian in chiral  $SU(3)$  model within the mean field approximation (MFA). Chiral  $SU(3)$  models have been widely used in the study of nuclear matter, finite nuclei, and hyperonic matter. The properties of the vector mesons in nuclear medium, and the energies of the kaons (antikaons) in the asymmetric nuclear matter were also studied using this model [15].

In the present work we have not considered the nucleon-antinucleon ( $n - \bar{n}$ ) excitation effect (Dirac sea), which is ultra-violet divergent. We have taken only the medium dependent part while calculating the spectral

<sup>a</sup> e-mail: pc\_raje@yahoo.com

function of the vector meson and the presence of at least one on-shell nucleon propagator provides a natural ultraviolet cut-off for the theory. As a result there does not arise any need for the addition of counter terms for the renormalization of the theory.

There is an enhancement of effective mass for  $\rho^{+,0}$ , whereas a reduction is seen for  $\rho^-$  at the maximum value of the asymmetry (neutron matter). The fact that the neutron and proton densities are different, brings in a modification of the propagation of  $\rho^{\pm,0}$  mesons in hot and dense asymmetric nuclear matter. The remarkable splitting of the spectral functions of the  $\rho$  meson triplets, when the discrete isospin symmetry is broken is revealed.

We organize the paper as follows: sect. 2 gives a brief description of the chiral  $SU(3)$  model used in the present investigation. Section 3 discusses the effects of finite temperature, asymmetry and density on the spectral function of the  $\rho$  meson. Section 4 contains the results and discussion and in sect. 5 we summarize our main findings of the present investigation.

## 2 The hadronic chiral $SU(3) \times SU(3)$ model

The effective hadronic chiral Lagrangian density used in the present work is given as

$$L = L_{kin} + \sum_{W=X,Y,V,A,u} L_{BW} + L_{vec} + L_0 + L_{SB}. \quad (1)$$

Equation (1) corresponds to a relativistic model of baryons and mesons adopting a nonlinear realization of chiral symmetry [16–19] and broken scale invariance [20–22] as a description of the hadronic matter. The model was used successfully to describe nuclear matter, finite nuclei, hypernuclei and neutron stars. The Lagrangian contains the baryon octet, the spin-0 and spin-1 meson multiplets as the elementary degrees of freedom. Here,  $L_{kin}$  is kinetic energy term,  $L_{BW}$  is the baryon-meson interaction term in which the baryons-spin-0 meson interaction term generates the baryon masses.  $L_{vec}$  describes the dynamical mass generation of the vector mesons via couplings to the scalar mesons and contains additionally quartic self-interactions of the vector fields.  $L_0$  contains the meson-meson interaction terms inducing the spontaneous breaking of chiral symmetry as well as a scale invariance breaking logarithmic potential.  $L_{SB}$  describes the explicit chiral symmetry breaking.

Baryon-scalar meson interactions generate the baryon masses through the coupling of the baryons to the non-strange  $\sigma$ , the strange  $\zeta$  scalar mesons and also to scalar-isovector meson  $\delta$ . The  $\delta$  meson is responsible for splitting of proton and neutron effective masses. The parameters  $g_1^S$ ,  $g_8^S$  and  $\alpha_S$  are adjusted to fix the baryon masses to their experimentally measured vacuum values. It should be emphasized that the nucleon mass also depends on the *strange condensate*  $\zeta$ . For the special case of ideal mixing ( $\alpha_S = 1$  and  $g_1^S = \sqrt{6}g_8^S$ ) the nucleon mass depends only on the non-strange quark condensate.

In analogy to the baryon-scalar meson coupling there exist two independent baryon-vector meson interaction terms corresponding to the F-type (antisymmetric) and D-type (symmetric) couplings. Here we will use the antisymmetric coupling, because the universality principle [23] and the vector meson dominance model suggest that the symmetric coupling should be small. Additionally, we choose the parameters [16,17,19] so as to decouple the strange vector field  $\phi_\mu \sim \bar{s}\gamma_\mu s$  from the nucleon, corresponding to an ideal mixing between  $\omega$  and the  $\phi$ -mesons. A small deviation of the mixing angle from ideal mixing has not been taken into account in the present investigation.

The concept of broken scale invariance leading to the trace anomaly in (massless) QCD,  $\theta_\mu^\mu = (\beta_{QCD}/2g)\langle G_{\mu\nu}^a G^{a,\mu\nu} \rangle$ , where  $G_{\mu\nu}^a$  is the gluon field strength tensor of QCD, is simulated in the effective Lagrangian at tree level [20–22] through the introduction of the scale breaking terms

$$L_{scalebreak} = -\frac{1}{4}\chi^4 \ln \frac{\chi^4}{\chi_0^4} + \frac{d}{3}\chi^4 \ln \left( \left( \frac{I_3}{\det(X)_0} \right) \left( \frac{\chi}{\chi_0} \right)^3 \right) \quad (2)$$

where  $I_3 = \det(X)$  with  $X$  as the multiplet for the scalar mesons. The effect of these logarithmic terms is to break the scale invariance, which leads to the trace of the energy momentum tensor as

$$\theta_\mu^\mu = (1-d)\chi^4. \quad (3)$$

Hence the scalar gluon condensate of QCD ( $\langle G_{\mu\nu}^a G^{a,\mu\nu} \rangle$ ) is simulated by a scalar dilaton field in the present hadronic model.

The hadronic properties are studied in the hot and dense asymmetric medium within the mean field approximation, where all the meson fields are treated as classical fields. Also in this approximation, only the scalar and the vector fields contribute to the baryon-meson interaction,  $L_{BW}$ , since for all other mesons, the expectation values are zero. The effects of the isospin asymmetry is introduced through the scalar-isovector  $\delta$  field and the isospin asymmetry parameter  $\eta$  is defined as  $\eta = \frac{1}{2}(\rho_N - \rho_P)/\rho_B$ , where  $\rho_N$  and  $\rho_P$  are the number densities of the neutron and the proton and  $\rho_B = \rho_N + \rho_P$ , is the total baryon density.

The Lagrangian density in the MFA has the following terms:

$$\begin{aligned} L_{BX} + L_{BV} &= - \sum_i \bar{\psi}_i [g_{i\omega}\gamma_0\omega + g_{i\rho}\gamma_0\rho + g_{i\phi}\gamma_0\phi + M_i^*] \psi_i, \\ L_{vec} &= \frac{1}{2} \frac{\chi^2}{\chi_0^2} (m_\omega^2\omega^2 + m_\rho^2\rho^2 + m_\phi^2\phi^2) \\ &\quad + g_4^4 (\omega^4 + 6\omega^2\rho^2 + \rho^4 + 2\phi^4), \\ L_0 &= -\frac{1}{2}k_0\chi^2 (\sigma^2 + \zeta^2 + \delta^2) + k_1 (\sigma^2 + \zeta^2 + \delta^2)^2 \\ &\quad + k_2 \left( \frac{\sigma^4}{2} + \frac{\delta^4}{2} + \zeta^4 + 3\sigma^2\delta^2 \right) \end{aligned}$$

$$\begin{aligned}
& +k_3\chi(\sigma^2 - \delta^2)\zeta - k_4\chi^4 \\
& -\frac{1}{4}\chi^4 \ln \frac{\chi^4}{\chi_0^4} + \frac{d}{3}\chi^4 \ln \left( \frac{(\sigma^2 - \delta^2)\zeta}{\sigma_0^2\zeta_0} \left( \frac{\chi}{\chi_0} \right)^3 \right), \\
L_{SB} = & -\left( \frac{\chi}{\chi_0} \right)^2 \left[ m_\pi^2 f_\pi \sigma \right. \\
& \left. + \left( \sqrt{2}m_K^2 f_K - \frac{1}{\sqrt{2}}m_\pi^2 f_\pi \right) \zeta \right], \quad (4)
\end{aligned}$$

where  $M_i^* = -g_{\sigma i}\sigma - g_{\zeta i}\zeta - g_{\delta i}\delta$  is the effective mass of the baryon of species  $i$ . Here  $k_0, k_1, k_2, k_3, k_4, \delta$  and  $g_4$  are parameters corresponding to the Mean-field and the Hartree approximations in the chiral  $SU(3)$  model. The thermodynamical potential of the grand canonical ensemble  $\Omega$  per unit volume  $V$  at a given chemical potential  $\mu_i$  and temperature  $T$  can be written as

$$\begin{aligned}
\frac{\Omega}{V} = & -L_{vec} - L_0 - L_{SB} - \nu_{vac} \\
& -T \frac{\gamma_i}{(2\pi)^3} \int d^3p \left[ \ln \left( 1 + e^{-\frac{1}{T}[E_i^*(p) - \mu_i^*]} \right) \right]. \quad (5)
\end{aligned}$$

Here  $\nu_{vac}$  is the vacuum energy (the potential at  $\rho = 0$ ) that has been subtracted in order to obtain a vanishing vacuum energy [20],  $\gamma_i$  are the spin-isospin degeneracy factor, and  $\gamma_i = 2$  for asymmetric nuclear matter. where,  $E_i^* = \sqrt{p^2 + M_i^{*2}}$  and  $\mu_i^* = \mu_i - g_{i\omega}\omega - g_{i\rho}\rho - g_{i\phi}\phi$  are the single particle energy and the effective chemical potential for the nucleon of species  $i$ . The mesonic field equations are determined by minimizing the thermodynamic potential. We shall use the frozen glueball approximation ( $\chi = \chi_0$ ), since the dilaton field which simulates the gluon condensate changes very little in the medium. We then have coupled equations only for the fields  $\sigma, \zeta, \delta$  and  $\omega$  as given by

$$\begin{aligned}
\frac{\partial(\Omega/V)}{\partial\sigma} = & k_0\chi^2\sigma - 4k_1(\sigma^2 + \zeta^2 + \delta^2)\sigma \\
& -2k_2(\sigma^3 + 3\sigma\delta^2) - 2k_3\chi\sigma\zeta - \frac{d}{3}\chi^4 \left( \frac{2\sigma}{\sigma^2 - \delta^2} \right) \\
& + m_\pi^2 f_\pi + \sum_i \frac{\partial M_i^*}{\partial\sigma} \rho_i^S = 0, \quad (6)
\end{aligned}$$

$$\begin{aligned}
\frac{\partial(\Omega/V)}{\partial\zeta} = & k_0\chi^2\zeta - 4k_1(\sigma^2 + \zeta^2 + \delta^2)\zeta - 4k_2\zeta^3 \\
& -k_3\chi(\sigma^2 - \delta^2) - \frac{d\chi^4}{3\zeta} + \frac{\partial M_i^*}{\partial\zeta} \rho_i^S \\
& + \left[ \sqrt{2}m_K^2 f_K - \frac{1}{\sqrt{2}}m_\pi^2 f_\pi \right] = 0, \quad (7)
\end{aligned}$$

$$\begin{aligned}
\frac{\partial(\Omega/V)}{\partial\delta} = & k_0\chi^2\delta - 4k_1(\sigma^2 + \zeta^2 + \delta^2)\delta \\
& -2k_2(\delta^3 + 3\delta\sigma^2) + k_3\chi\delta\zeta - \frac{d}{3}\chi^4 \left( \frac{2\delta}{\sigma^2 - \delta^2} \right) \\
& + \sum_i \frac{\partial M_i^*}{\partial\delta} \rho_i^S = 0, \quad (8)
\end{aligned}$$

$$\frac{\partial(\Omega/V)}{\partial\omega} = -m_\omega^2\omega - 4g_4^4\omega^3 + g_{N\omega}\rho_i = 0, \quad (9)$$

which have to be solved self-consistently to obtain the values of  $\sigma, \zeta, \delta$  and  $\omega$ . Here  $\rho_i^S$  and  $\rho_i$  are the scalar and vector densities for the nuclear matter at finite temperature,  $T$  given as

$$\begin{aligned}
\rho_i^S = & \gamma_i \int \frac{d^3p}{(2\pi)^3} \frac{M_i^*}{E_i^*} (n_i(p) + \bar{n}_i(p)), \\
\rho_i = & \gamma_i \int \frac{d^3p}{(2\pi)^3} (n_i(p) - \bar{n}_i(p)). \quad (10)
\end{aligned}$$

The  $n_i$  and  $\bar{n}_i$  are the thermal distribution functions for the neutron (proton) and the antineutron (antiproton) respectively,

$$n_i(p) = \frac{1}{e^{(E_i^* - \mu_i^*)/T} + 1}, \quad \bar{n}_i(p) = \frac{1}{e^{(E_i^* + \mu_i^*)/T} + 1}. \quad (11)$$

### 3 Rho-meson spectral function in asymmetric nuclear matter

The hadronic matter produced in ultra-relativistic heavy-ion collisions at very high densities and temperatures is studied using the finite temperature field theory [24, 25]. In the present calculation thermal effects enter through thermal neutron and proton loops. In Minkowski space, the self-energy of the  $\rho$  vector meson can be expressed as [8, 26]

$$\Pi^{\mu\nu}(k) = \Pi_L(k)P_L^{\mu\nu} + \Pi_T(k)P_T^{\mu\nu}, \quad (12)$$

where  $k^2 = k_0^2 - |\mathbf{k}^2|$ . The  $P_L^{\mu\nu}$  and  $P_T^{\mu\nu}$  are the longitudinal and the transverse projection tensors defined as

$$\begin{aligned}
P_T^{00} = P_T^{0i} = P_T^{i0} = & 0, \quad P_T^{ij} = \delta^{ij} - \frac{k_i k_j}{|\mathbf{k}^2|}, \\
P_L^{\mu\nu} = & \frac{k^\mu k^\nu}{k^2} - g^{\mu\nu} - P_T^{\mu\nu}. \quad (13)
\end{aligned}$$

$\Pi_L$  and  $\Pi_T$  are related to the components of the self-energy by [27]

$$\Pi_L(k) = \frac{k^2}{|\mathbf{k}^2|} \Pi^{00}(k), \quad \Pi_T(k) = -\frac{1}{2} (\Pi_\mu^\mu + \Pi_L(k)). \quad (14)$$

The imaginary part of the retarded propagator is referred to as the spectral function. The study of the  $\rho$  meson spectral function is attributed to calculating the in-medium self-energy of the  $\rho$  meson.

#### 3.1 $\rho$ NN interaction

The contribution of nucleon excitations through nucleon-loop to  $\rho$  self-energy is analyzed in terms of the effective Lagrangian density [28]

$$L_{\rho NN} = g_{\rho NN} \left( \bar{\Psi} \gamma_\mu \tau^a \Psi V_a^\mu - \frac{\kappa_\rho}{2M_i} \bar{\Psi} \sigma_{\mu\nu} \tau^a \Psi \partial^\nu V_a^\mu \right), \quad (15)$$

where  $V_a^\mu$  is the  $\rho$  meson field and  $\Psi$  is the nucleon field. The second order polarization function or the self-energy can be written as

$$\Pi_{\mu\nu}^{\rho NN} = -ig_{\rho NN}^2 \int \frac{d^4 p}{(2\pi)^4} \text{Tr} [\Gamma_\mu(k) G(p+k) \Gamma_\nu(-k) G(p)], \quad (16)$$

where

$$\Gamma^\mu(k) = \gamma^\mu + \frac{i\kappa_\rho}{2M_i} \sigma_{\mu\nu} k^\nu, \quad (17)$$

with  $\sigma_{\mu\nu} = \frac{i}{2}[\gamma_\mu, \gamma_\nu]$ ,  $M_i$  and  $M_i^*$  are the neutron (proton) masses in vacuum and in the hot hadronic medium respectively.  $G(p)$  is the nucleon propagator in matter which can be written as

$$G(p) = (p + M_i^*) \left\{ \frac{1}{p^2 - M_i^{*2}} + i\pi\delta(p^2 - M_i^{*2}) [\theta(p_0)n_i(p) + \theta(-p_0)\bar{n}_i(p)] \right\}. \quad (18)$$

The polarization tensor  $\Pi_{\mu\nu}^{\rho NN}(k)$  can be separated into two parts,

$$\Pi_{\mu\nu}^{\rho NN}(k) = - \left( g_{\mu\nu} - \frac{k_\mu k_\nu}{k^2} \right) \Pi_F^{\rho NN}(k) + \Pi_{D,\mu\nu}^{\rho NN}(k), \quad (19)$$

corresponding to the vacuum and the matter contributions. Using dimensional regularization and taking a phenomenological subtraction procedure [28], the vacuum part ( $T = 0$ ) is

$$\Pi_{iF,L(T)}^{\rho NN}(k) = k^2 \left( \frac{g_{\rho NN}}{\pi} \right)^2 \left( I_1 + \frac{\kappa_\rho M_i^*}{2M_i} I_2 + \left( \frac{\kappa_\rho}{2M_i} \right)^2 \frac{k^2 I_1 + M_i^{*2} I_2}{2} \right), \quad (20)$$

where

$$I_1 = \int_0^1 dx x(1-x) \ln C, \quad I_2 = \int_0^1 dx \ln C, \quad (21)$$

$$C = \frac{M_i^{*2} - x(1-x)k^2}{M_i^2 - x(1-x)k^2}.$$

The polarization tensor for  $\rho^{(0,\pm)}$  will be the same for symmetric nuclear matter and the condition for current conservation ( $k^\mu \Pi_{\mu\nu} = \Pi_{\mu\nu} k^\nu = 0$ ) is automatically fulfilled. Even when the nuclear matter is asymmetric, the current is conserved for  $\rho^0$  as it involves only the  $p - p$  and  $n - n$  loops. *i.e.*,  $\rho^0$  is blind to isospin asymmetry. But for the  $\rho^\pm$  as they involve the  $p - n$  loop, when the isospin symmetry is broken, the current is only partially conserved. The Fermi sea polarization function  $\Pi_{\mu\nu}^D$  consists of the vector-vector, vector-tensor, and tensor-tensor contributions and hence can be expressed as

$$\Pi_{\mu\nu}^D(k) = \Pi_{\mu\nu}^{vv}(k) + \Pi_{\mu\nu}^{vt}(k) + \Pi_{\mu\nu}^{tt}(k). \quad (22)$$

The real part of the temperature-density dependent polarization tensor in the region of stable collective modes for  $\rho^+$  is given by

$$\Pi_{\mu\nu}^D(k) = g_{\rho NN}^2 \left\{ \int \frac{d^4 p}{(2\pi)^4} 2\pi\delta(p^2 - M_N^{*2}) \frac{\tau_{\mu\nu}(p, p+k)}{(p+k)^2 - M_N^{*2}} [\theta(p_0)n_N(p) + \theta(-p_0)\bar{n}_N(p)] \right\} + g_{\rho NN}^2 \left\{ \int \frac{d^4 p}{(2\pi)^4} 2\pi\delta(p^2 - M_P^{*2}) \frac{\tau_{\mu\nu}(p-k, p)}{(p-k)^2 - M_P^{*2}} [\theta(p_0)n_P(p) + \theta(-p_0)\bar{n}_P(p)] \right\}, \quad (23)$$

where

$$\tau_{\mu\nu}(p-k, p) = \tau_{\mu\nu}^{vv}(p-k, p) + \tau_{\mu\nu}^{vt}(p-k, p) + \tau_{\mu\nu}^{tt}(p-k, p) \quad (24)$$

and

$$\tau_{\mu\nu}^{vv}(p-k, p) = 4[(p-k)_\mu p_\nu + p_\mu(p-k)_\nu - (p-k) \cdot p g_{\mu\nu} + M_P^{*2} g_{\mu\nu}],$$

$$\tau_{\mu\nu}^{vt}(p-k, p) = 4M_P^* \frac{\kappa_\rho}{M} q^2 K_{\mu\nu},$$

$$\tau_{\mu\nu}^{tt}(p-k, p) = 16 \left( \frac{\kappa_\rho}{4M_P^*} \right)^2 [K_{\mu\nu} \{ 2(p \cdot k)^2 - p^2 k^2 - k^2(p \cdot k) - k^2 M_P^{*2} \} - 2k^2 P_{\mu\nu}]. \quad (25)$$

Here  $K_{\mu\nu} = -g_{\mu\nu} + \frac{k_\mu k_\nu}{k^2}$  and

$$P_{\mu\nu} = \left\{ p_\mu - \left( \frac{p \cdot k}{k^2} \right) k_\mu \right\} \left\{ p_\nu - \left( \frac{p \cdot k}{k^2} \right) k_\nu \right\}.$$

It can be seen that due to the symmetry breaking, the vector current is not conserved for the  $\rho^\pm$ . An evaluation of the polarization tensor shows that  $k^\mu \Pi_{\mu\nu}^D \neq 0$  as required by the current conservation. By using the techniques of current algebra, it has been shown in [13] that apart from the fluctuation, there arises an additional contribution to the current, which is proportional to the difference between the neutron and the proton number densities, when the ground state does not respect the  $p \leftrightarrow n$  symmetry, *i.e.*  $k^\mu \Pi_{\mu\nu}^D = 2g_{\rho NN}^2 (\rho_N - \rho_P) \delta_{0\nu}$  for  $\rho^+$ . So a redefinition of the polarization tensor is required for studying the vector meson propagation in asymmetric nuclear matter. The modified polarization tensor in the case of the vector meson interacting with real particle-hole excitations in the nuclear medium is given by

$$\tilde{\Pi}_{\mu\nu} = \Pi_{\mu\nu} \mp \frac{2g_{\rho NN}^2 (\rho_N - \rho_P)}{k_0} \delta_{0\mu} \delta_{0\nu}, \quad (26)$$

for  $\rho^\pm$ . For  $\rho^+$ , the results are

$$\begin{aligned}
(\Pi_\mu^\mu)^{D,vv} &= \left( \frac{g_{\rho NN}^2}{2\pi^2} \right) \int_0^\infty \frac{p^2 dp}{E_P^*(k)} \frac{1}{p|\mathbf{k}|} (n_P + \bar{n}_P) \\
&\quad [(2M_P^{*2} + k^2) \ln a - 4p|\mathbf{k}|] \\
&\quad + \left( \frac{g_{\rho NN}^2}{2\pi^2} \right) \int_0^\infty \frac{p^2 dp}{E_N^*(k)} \frac{1}{p|\mathbf{k}|} (n_N + \bar{n}_N) \\
&\quad [(2M_N^{*2} + k^2) \ln b - 4p|\mathbf{k}|] \\
(\Pi_\mu^\mu)^{D,vt} &= -\frac{3g_{\rho NN}^2}{\pi^2} \left( \frac{k^2}{|\mathbf{k}|} \right) \frac{\kappa_\rho M_P^*}{2M} \int_0^\infty \frac{p dp}{E_P^*(k)} \\
&\quad (n_P + \bar{n}_P) \ln a \\
&\quad - \frac{3g_{\rho NN}^2}{\pi^2} \left( \frac{k^2}{|\mathbf{k}|} \right) \frac{\kappa_\rho M_N^*}{2M} \int_0^\infty \frac{p dp}{E_N^*(k)} \\
&\quad (n_N + \bar{n}_N) \ln b \\
(\Pi_\mu^\mu)^{D,tt} &= \left( \frac{g_{\rho NN}^2}{4\pi^2} \right) \left( \frac{\kappa_\rho}{M} \right)^2 \int_0^\infty \frac{p^2 dp}{E_P^*(k)} (n_P + \bar{n}_P) \\
&\quad \left[ \frac{k^2}{4p|\mathbf{k}|} \{ (k^2 + 8M_P^{*2}) \ln a - 4p|\mathbf{k}| \} + 4E_P^* k_0 \right] \\
&\quad + \left( \frac{g_{\rho NN}^2}{4\pi^2} \right) \left( \frac{\kappa_\rho}{M} \right)^2 \int_0^\infty \frac{p^2 dp}{E_N^*(k)} (n_N + \bar{n}_N) \\
&\quad \left[ \frac{k^2}{4p|\mathbf{k}|} \{ (k^2 + 8M_N^{*2}) \ln b - 4p|\mathbf{k}| \} - 4E_N^* k_0 \right].
\end{aligned} \tag{27}$$

The redefined polarization tensor calculated using eq. (26) now fullfils the condition of current conservation.  $\Pi_L$  and  $\Pi_T$  are calculated using eq. (14). We have shown only the results for the  $\rho^+$  meson.  $\rho^-$  being the anti-particle, the results can be obtained by replacing  $k_0$  with  $-k_0$  and  $|\mathbf{k}|$  with  $-|\mathbf{k}|$  and  $P \rightarrow N$ . From the expressions it is clear that the polarization tensors are modified differently for the different members of the multiplet and this subtle requirement when not considered would lead to unphysical splitting of the transverse and the longitudinal modes.

Here  $p = |\mathbf{p}|$ .  $\mathbf{k}$  is the 3-momentum of the vector meson,  $\rho$ .  $a$  and  $b$  are defined as

$$\begin{aligned}
a &= \frac{k^2 + 2p|\mathbf{k}| - 2E_P^* k_0}{k^2 - 2p|\mathbf{k}| - 2E_P^* k_0}, \\
b &= \frac{k^2 + 2p|\mathbf{k}| + 2E_N^* k_0}{k^2 - 2p|\mathbf{k}| + 2E_N^* k_0}.
\end{aligned} \tag{28}$$

The real and the imaginary parts are calculated by performing the analytic continuation  $k_0 \rightarrow E + i\varepsilon$ , where,  $E = \sqrt{M_\rho^2 + |\mathbf{k}|^2}$ ,  $M_\rho$  being the invariant mass of the  $\rho$  in the medium. The spectral function is obtained as

$$A_{L(T)} = -\frac{\text{Im } \Pi_{L(T)}}{[M_\rho^2 - (m_\rho^2 + \text{Re } \Pi_{L(T)})]^2 + [\text{Im } \Pi_{L(T)}]^2}, \tag{29}$$

where  $\Pi_{L(T)}$  corresponds to the particular member of the triplet. Imaginary parts exist for  $M_\rho \geq (M_N^* + M_P^*)$  [11, 9] for  $\rho^\pm$  and  $M_\rho \geq 2M^*$  for  $\rho^0$ .

## 4 Results and discussions

The results of the calculations for the spectral function of the  $\rho$  multiplet in the hot and dense asymmetric nuclear matter are presented in this section. It is clearly emphasized that the present phenomenological model is intended to study only the effects of the decreasing neutron and proton effective masses with neutron and proton densities on the  $\rho$ -meson spectral function in the medium. Also any other decay channels which can contribute to the real and the imaginary parts are neglected here. In the present model the effects of the finite neutron (proton) density enters through the nucleon loops. From the plots of the spectral function it will be evident that this is an important effect. The decreasing effective neutron (proton) mass with density and asymmetry considerably changes the  $\rho$ -meson spectral function.

In the chiral  $SU(3)$  model the parameters used in the calculation of the effective neutron (proton) masses and the corresponding effective chemical potentials are,  $m_\pi = 0.1396$  GeV,  $m_K = 0.498$  GeV,  $m_\omega = 0.783$  GeV,  $f_\pi = 0.0933$  GeV,  $f_K = 0.122$  GeV,  $\zeta_0 = 0.10656$  GeV,  $k_0 = 2.37$ ,  $k_1 = 1.4$ ,  $k_2 = -5.55$ ,  $k_3 = -2.64$ ,  $d = 0.064$ ,  $\chi_0 = 0.4027$  GeV,  $g_{\sigma N} = 10.6$ ,  $g_{\zeta N} = -0.47$ ,  $g_{\delta N} = 2.5$ ,  $g_4 = 2.7$  [21].

As mentioned above, the variation of the effective neutron (proton) mass and their effective chemical potentials determine the spectral function of the  $\rho$ -meson triplet in the hot and dense asymmetric nuclear matter. The nuclear matter saturation density is chosen to be  $\rho_0 = 0.15 \text{ fm}^{-3}$  [21]. Figure 1 depicts the variation of the effective masses of the  $\rho$  multiplet, the neutron and the proton against the scaled density for two different asymmetry parameter values and for two temperatures,  $T = 0$  and  $0.15$  GeV within MFA. For the same temperature, there is a considerable splitting in the effective masses of the  $\rho$  multiplet, when the asymmetry parameter is increased. Among the isospin multiplet, the  $\rho^+$  takes a larger mass,  $\rho^-$  lower mass with that of  $\rho^0$  in between. It can be seen that the change in the effective vector meson masses with the asymmetry parameter is larger than their modification with temperature.

The effect of the isospin asymmetry on the properties of the  $\rho$  vector meson can be understood in the limit of maximum asymmetry, *i.e.*  $\eta = 0.5$ , the neutron matter.

From fig. 2, it can be seen that for a particular value of the asymmetry parameter  $\eta$ , the effective masses  $M_i^*$ , (where  $i = p, n$ ) drop with the increase in density of the nuclear medium. This drop in the value of  $M_i^*$  with density is seen to be considerably larger than the modification of  $M_i^*$  due to temperature at a particular density. For the same density, if  $\eta$  is increased, the neutron and the proton masses become non-degenerate, the neutron (proton) mass is lowered (enhanced) and this non-degeneracy is increased with increase in density. The neutron and the

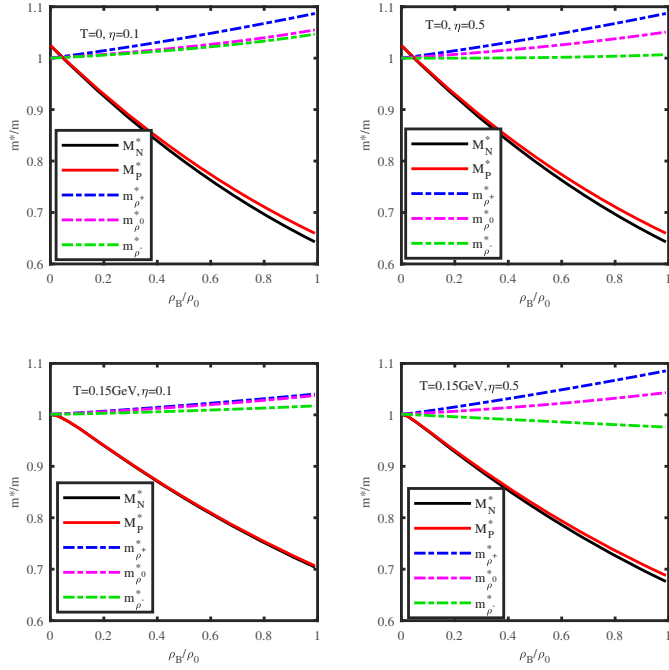


**Fig. 1.** Variation of  $\rho$  and nucleon effective masses against density for (a)  $T = 0$  and  $\eta = 0.1$ , (b)  $T = 0$  and  $\eta = 0.5$ , (c)  $T = 0.15$  GeV and  $\eta = 0.1$  and (d)  $T = 0.15$  GeV and  $\eta = 0.5$  within MFA in the chiral  $SU(3)$  model.

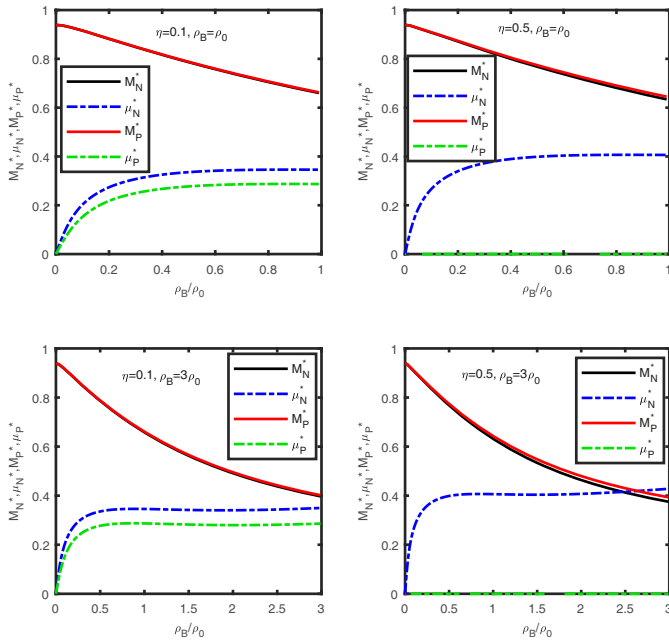


**Fig. 2.** Variation of nucleon effective masses and effective chemical potentials against density for (a)  $\rho_B = \rho_0$  and  $\eta = 0.1$ , (b)  $\rho_B = \rho_0$  and  $\eta = 0.5$ , (c)  $\rho_B = 3\rho_0$  and  $\eta = 0.1$  and (d)  $\rho_B = 3\rho_0$  and  $\eta = 0.5$  within MFA in the chiral  $SU(3)$  model.

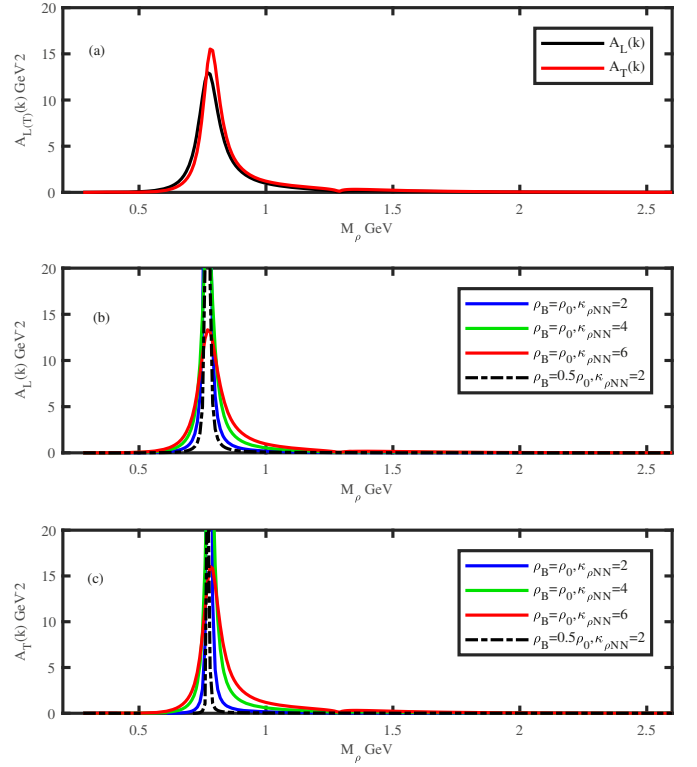


**Fig. 3.** Longitudinal and transverse spectral functions for the  $\rho$  against the invariant mass  $M_\rho$  for  $\rho_B = \rho_0$  in symmetric nuclear matter.  $|\mathbf{k}| = 0.75$  GeV and  $T = 0.15$  GeV.

proton effective chemical potentials  $\mu_N^*$  and  $\mu_P^*$  separate, with  $\mu_N^*$  going up and  $\mu_P^*$  going down with increasing  $\eta$ . This behaviour is due to the fact that at finite densities and for isospin asymmetric nuclear matter, the scalar-isovector field  $\delta$  contributes, whereas for isospin symmetric nuclear matter, the  $\delta$  field has no contribution. While the condensed scalar  $\sigma$  and  $\zeta$  meson fields generate a shift of the nucleon mass, the  $\delta$ -meson is responsible for the splitting of proton and neutron effective masses. The  $\delta$ -meson is considered to be an useful degree of freedom in the description of asymmetric nuclear matter.

The present work is limited to the discussion of the effects of the density and asymmetry on the spectral function of the  $\rho$  multiplet. The parameters chosen in the calculation of the spectral function are,  $m_\rho = 0.77$  GeV,  $g_{\rho NN}^2 = 6.96$ , and  $\kappa_{\rho NN} = 6.1$ . The coupling constants  $g_{\rho NN}$  and  $\kappa_{\rho NN}$  are determined from the fitting to the nucleon-nucleon scattering data done by the Bonn group [29].

Figures 3, 4, and 5 plot the longitudinal and the transverse spectral functions for the  $\rho$  meson in the symmetric and asymmetric cases. For  $\eta = 0$ , the longitudinal and the transverse peaks are at 0.77 GeV and 0.78 GeV respectively, at a  $\rho$  propagation momentum  $|\mathbf{k}| = 0.75$  GeV for  $\rho_B = \rho_0$ . For a small asymmetry,  $\eta = 0.1$ , in the left panel (fig. 4), there is a very small splitting between the longitudinal and the transverse spectral functions among the  $\rho$  multiplet. The longitudinal spectral function peaks for the  $\rho^0$  and the  $\rho^-$  are at 0.77 GeV, but that for  $\rho^+$

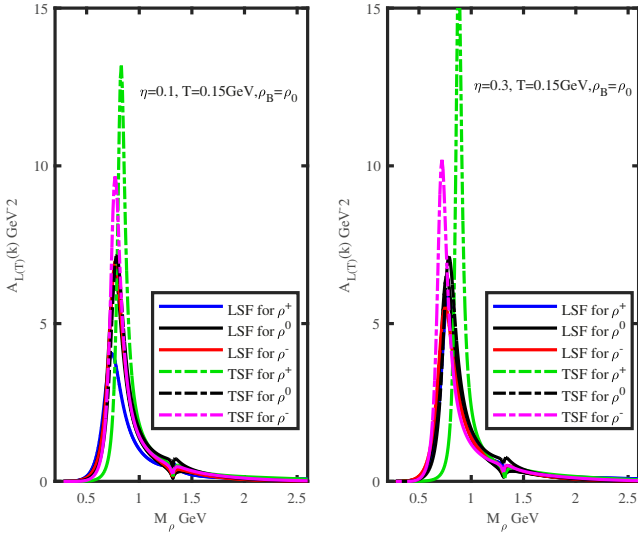


**Fig. 4.** Longitudinal and transverse spectral functions for the  $\rho$  multiplet against the invariant mass  $M_\rho$  for  $\rho_B = \rho_0$  for two different asymmetry parameters  $\eta = 0.1$  and  $0.3$  respectively.  $|\mathbf{k}| = 0.75$  GeV and  $T = 0.15$  GeV.

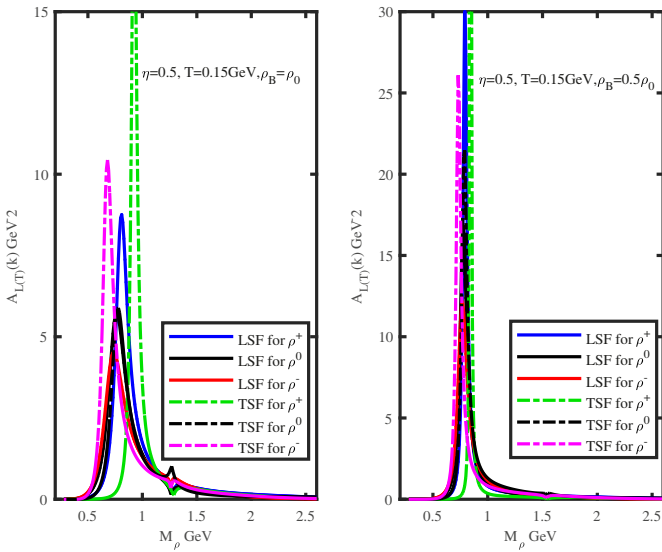


**Fig. 5.** Longitudinal and transverse spectral functions for the  $\rho$  multiplet against the invariant mass  $M_\rho$  for  $\eta = 0.5$  (neutron matter) for two densities  $\rho_B = \rho_0$  and  $\rho_B = 0.5\rho_0$ .  $|\mathbf{k}| = 0.75$  GeV and  $T = 0.15$  GeV.

is at a lower value of  $0.74$  GeV. The transverse spectral function peaks separate with  $\rho^+$  taking a higher  $M_\rho$  value than  $\rho^-$  while that of  $\rho^0$  lies in between.

From figs. 4 and 5, one can see that for low values of  $\eta$ ,  $A_L(k)$  peak for  $\rho^+$  is at a lower  $M_\rho$ , while that for  $\rho^0$  and  $\rho^-$  are degenerate. But with an increase in  $\eta$ , the peaks clearly split with that of  $\rho^+$  taking higher  $M_\rho$  values. The peak for  $\rho^0$  lies in between those for  $\rho^+$  and  $\rho^-$ . The splitting between the transverse and the longitudinal modes of the multiplet is seen to increase with increasing values of the asymmetry.

Now consider the extreme limit of asymmetry, *i.e.* the neutron matter, in fig. 5. There is a clear separation of both the modes among the isospin multiplet. For  $\eta = 0.5$ ,  $\rho_P = 0$  which implies  $n_p = \bar{n}_p$  as  $\mu_P^* = 0$ , at finite  $T$ . So considering the Fermi sea contribution alone, for  $\rho^+$ , one can see that the virtual proton propagator modification is due to temperature alone, whereas for the virtual neutron propagator, modification is due to both density and temperature.  $\rho^+$  and  $\rho^-$  will be modified differently as for  $\rho^+$ , the contribution is due to  $p - n_h$  whereas for  $\rho^-$ , the contribution is due to  $n - p_h$ . In the case of  $\rho^0$ , the contributions are from  $n - n_h$  and  $p - p_h$ . It can be inferred that the modification of propagators of the members of the multiplet is different for a given asymmetry which results in the different contribution from different loops involved. From figs. 4 and 5, it is evident that the splitting among the different members of the multiplet and thereby the splitting of the transverse and the longitudinal modes are highly dependent on the density of the nuclear matter as well as the asymmetry of the medium. For small asymmetry, longitudinal spectral density for  $\rho^+$  is wider. With increasing asymmetry, the contribution from the particle-hole sea ( $p - n_h$ ) becomes large and at maximum asymmetry the baryon density is entirely due to neutron alone. The spectral function plot becomes narrower implying a lower decay width and more stability. The transverse spectral density is very narrow for low asymmetry which approaches a  $\delta$ -function for maximum asymmetry implying high stability. At the extreme value of asymmetry, for  $\rho^-$  as mentioned above, there is no density contribution to the virtual proton propagator. This is reflected in the spectral function plots of  $\rho^-$ , with  $A_L(k)$  getting broader and  $A_T(k)$  getting narrower, implying different behaviour of  $A_L(k)$  and  $A_T(k)$ . For maximum asymmetry, the longitudinal spectral density for  $\rho^-$  is wider than that for  $\rho^0$  and  $\rho^+$  showing the instability of  $\rho^-$  in this mode. The transverse spectral density is wider for  $\rho^0$  than for  $\rho^\pm$ . Moreover, the  $A_T(k)$  peaks for  $\rho^0$  and  $\rho^+$  always lie above that for  $A_L(k)$ , while for  $\rho^-$ ,  $A_L(k)$  peak lies above that for  $A_T(k)$  except for low asymmetry values. This may be due to the different loops contributing differently for a given value of asymmetry as explained earlier.

Within MFA, as pointed in [11], the repulsion induced by the Fermi polarization shifts the spectral function to higher invariant mass values. But the imaginary part coming from the particle-hole sector ( $p - n_h$  for  $\rho^+$ ,  $n - p_h$  for  $\rho^-$  and  $n - n_h$ ,  $p - p_h$  for  $\rho^0$ ) is found to be different for the different members of the multiplet. This together with the change in the real part of the spectral function is responsible for the change in the width and the peak positions of the different members of the multiplet.

For  $\rho_B = 0.5\rho_0$ , there is only a small splitting in the longitudinal spectral density even for  $\eta = 0.5$ . The splitting in the transverse spectral density is significant among the isospin multiplets, showing the different behaviour of the longitudinal and the transverse modes with varying baryon density and asymmetry when the  $\rho$  is propagating with finite momentum in an asymmetric nuclear medium.

Figures 3(b) and (c) show the spectral density for running tensor coupling  $\kappa_{\rho NN}$ . Though the peaks always

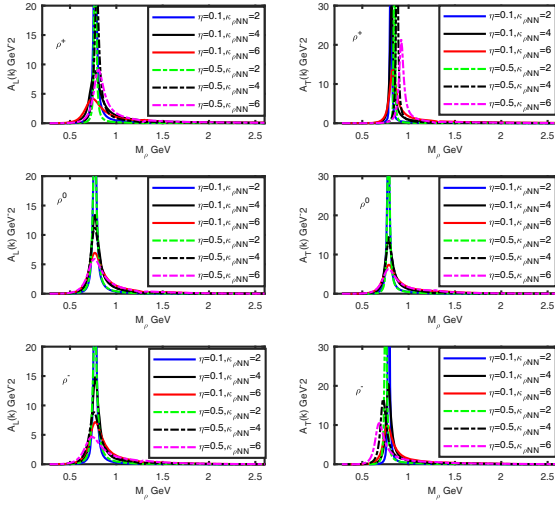


**Fig. 6.** Longitudinal and transverse spectral functions for the  $\rho$  multiplet against the invariant mass  $M_\rho$  for  $\rho_B = \rho_0$  for two different asymmetry parameters  $\eta = 0.1$  and  $0.5$  respectively.  $\kappa_{\rho NN} = 2, 4, 6$ ,  $|\mathbf{k}| = 0.75$  GeV and  $T = 0.15$  GeV.

remain at  $0.77$  GeV and  $0.78$  GeV for longitudinal and transverse modes in the three cases,  $\sqrt{m_\rho^2 + \text{Re } \Pi_{L(T)}}$  is different. For  $\kappa_{\rho NN} = 2$ ,  $\text{Re } \Pi_L$  is negative, whereas  $\text{Re } \Pi_T$  is positive. A positive value for  $\text{Re } \Pi_T$  implies a small increase in the effective mass, while a negative  $\text{Re } \Pi_L$ , a drop in the effective mass. For  $\kappa_{\rho NN} = 2$  and  $4$ , the peaks are very sharp, but for  $\kappa_{\rho NN} = 6$ , the peak widens implying the instability of  $\rho$  with increasing  $\kappa_{\rho NN}$  ( $-\text{Im } \Pi_{L(T)}$  increases with increasing  $\kappa_{\rho NN}$ ) within MFA. The transverse spectral function peaks are at  $0.78$  GeV and are less wider. For a small density  $\rho_B = 0.5\rho_0$ , the peaks almost approach a  $\delta$ -function for  $\kappa_{\rho NN} = 2$ . One can observe that for very small densities, both the longitudinal and the transverse peaks coincide, while the  $\sqrt{m_\rho^2 + \text{Re } \Pi_L}$  and  $\sqrt{m_\rho^2 + \text{Re } \Pi_T}$  are slightly different. As  $-\text{Im } \Pi_T$  is always less than  $-\text{Im } \Pi_L$ , the longitudinal mode is wider than the transverse one and hence less stable.

In fig. 6, the longitudinal and the transverse spectral densities are presented at nuclear matter saturation density,  $\rho_B = \rho_0$  for  $\eta = 0.1$  and  $0.5$ . As in fig. 3,  $\kappa_{\rho NN}$  is considered as a running parameter. This is intended to show how sensitive the properties of the vector mesons are to the magnetic interaction. It has been shown in [13] that the effect of the magnetic interaction is to reduce the vector meson mass in relativistic Hartree approximation (RHA). But within MFA, the situation is different. Though the peaks for  $\rho^0$  are almost at the same  $M_\rho$  value for the symmetric and the asymmetric cases, those for  $\rho^+$  and  $\rho^-$  are highly displaced from the nominal pole mass value. From the plots for  $\rho^+$ , for small asymmetries,  $A_L(k)$  peaks are seen to shift to low invariant mass values with increasing  $\kappa_{\rho NN}$ . For the same  $\kappa_{\rho NN}$ , if we increase the

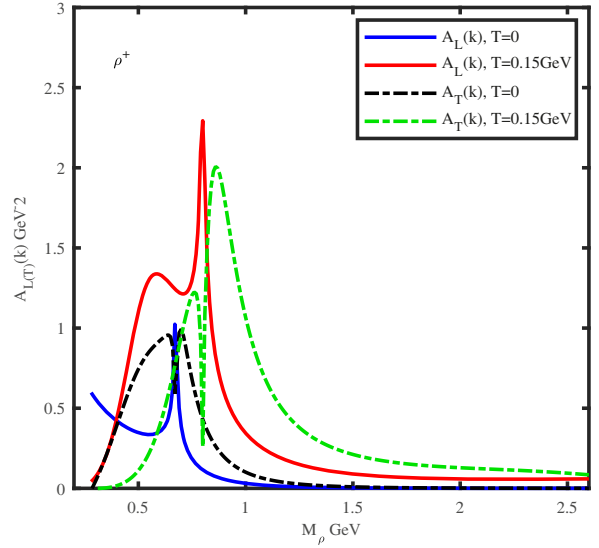


**Fig. 7.** Longitudinal and transverse spectral functions for  $\rho^+$  against the invariant mass  $M_\rho$ .  $\rho_B = 3\rho_0$ ,  $\eta = 0.05$ ,  $|\mathbf{k}| = 0.75$  GeV,  $T = 0$  and  $0.15$  GeV respectively.

value of  $\eta$ ,  $A_L(k)$  peaks shift to higher invariant mass region and become less wider denoting more stability. But for  $\rho^-$  the trend is opposite, with the peaks shifting to low invariant mass region for maximum asymmetry. The effects are clearly seen in the  $A_T(k)$  peaks in the right panel. For a given value of  $\kappa_{\rho NN}$ ,  $A_T(k)$  peaks shift to higher  $M_\rho$  values for  $\rho^+$ , whereas, they shift to lower  $M_\rho$  values for  $\rho^-$ .  $\rho^+$  is always more stable in both modes within MFA. It can also be inferred that the particles are more stable when  $g_{\rho NN} > \kappa_{\rho NN}$  within MFA. From the plots, one can observe that the transverse spectral density is more modified than the longitudinal mode in an isospin asymmetric nuclear medium. As explained earlier, this may be due to the different loops involved contributing differently for a given value of asymmetry. In effect, one can conclude that the tensor coupling splits the longitudinal and the transverse modes substantially.

Figures 7, 8, and 9 show the spectral densities of the triplet at  $\rho_B = 3\rho_0$  for  $T = 0$  and  $0.15$  GeV respectively for a very small asymmetry value  $\eta = 0.05$  within the MFA. Even at very small asymmetries, there is a huge difference in the qualitative behaviour of the transverse and the longitudinal components of the spectral function at very high density. One can observe that the original spectral distribution of the  $\rho$  gets broadened largely that it is no longer possible to interpret it as a good quasiparticle. A double-hump structure can be seen for the transverse spectral density for the isospin triplet at  $T = 0.15$  GeV. Such a behaviour was observed for the  $\rho$  meson in dense nuclear matter which includes baryon resonances  $N^*(1520)$  and  $N^*(1720)$  [30]. Moreover, the broadening of the spectral density shows an accumulation of strength over a wide range of  $M_\rho$ .

We are studying the temperature/density effects on the spectral density when the propagation momentum

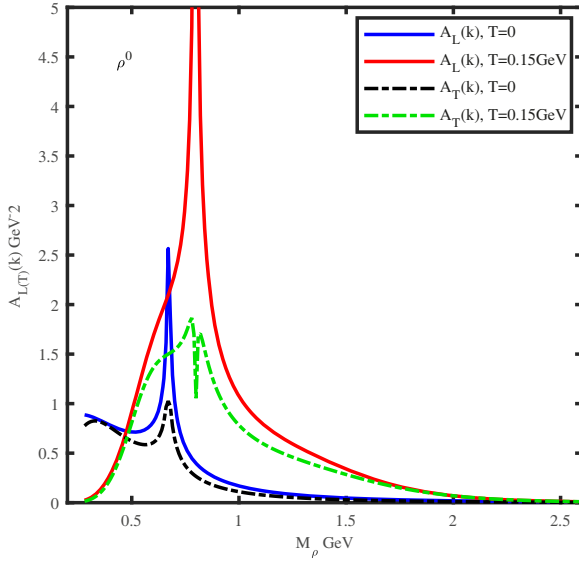


**Fig. 8.** Longitudinal and transverse spectral functions for  $\rho^0$  against the invariant mass  $M_\rho$ .  $\rho_B = 3\rho_0$ ,  $\eta = 0.05$ ,  $|\mathbf{k}| = 0.75$  GeV,  $T = 0$  and  $0.15$  GeV respectively.

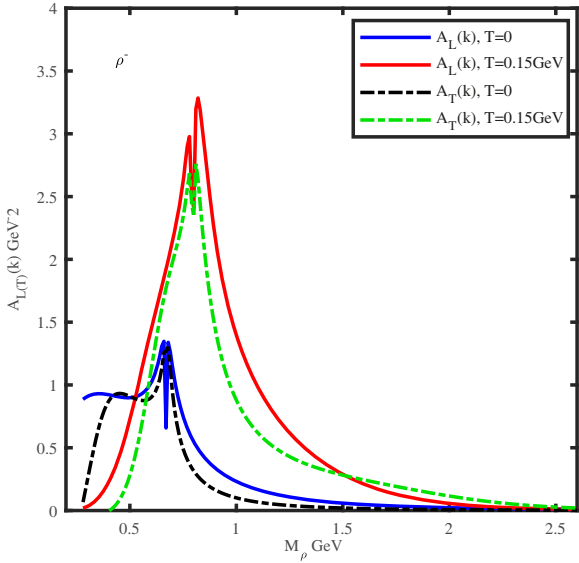


**Fig. 9.** Longitudinal and transverse spectral functions for  $\rho^-$  against the invariant mass  $M_\rho$ .  $\rho_B = 3\rho_0$ ,  $\eta = 0.05$ ,  $|\mathbf{k}| = 0.75$  GeV,  $T = 0$  and  $0.15$  GeV respectively.

of the  $\rho$  meson is very small and the results are depicted in fig. 10 for the nuclear saturation density  $\rho_0$ . For  $\eta = 0$ , though there is a well-defined peak for  $A_L(k)$  at  $M_\rho = 0.46$  GeV, the transverse spectral function has a double-hump like structure beyond 1 GeV. There is also a large broadening of  $A_L(k)$ . For neutron matter ( $\eta = 0.5$ ), the peaks are at 0.41 GeV, 0.37 GeV, and 0.35 GeV for  $\rho^+$ ,  $\rho^0$ , and  $\rho^-$  respectively for  $A_L(k)$ , *i.e.* the peaks are highly shifted towards low invariant mass region. Finite density/temperature effects are found to decrease with

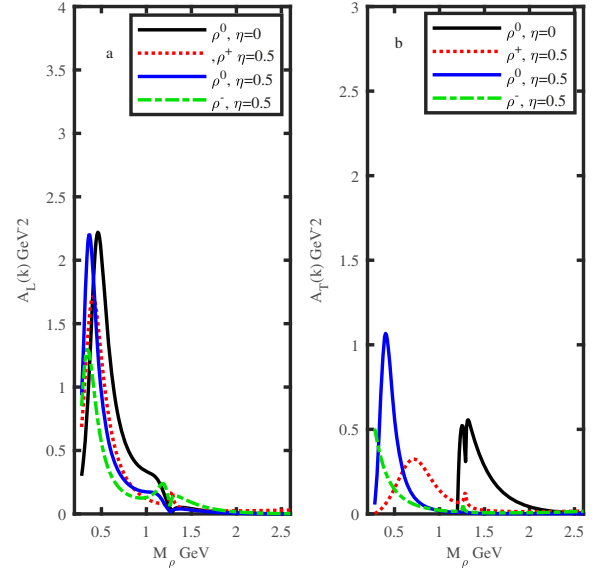


**Fig. 10.** Longitudinal and transverse spectral functions for the  $\rho$  multiplet for nucleon matter ( $\eta = 0$ ) and neutron matter ( $\eta = 0.5$ ) against the invariant mass  $M_\rho$ .  $\rho_B = \rho_0$ ,  $|\mathbf{k}| = 0.1$  GeV and  $T = 0.15$  GeV.

increasing momentum. This may be because of the increasing many-body effects when the distances involved are larger as low momentum means larger distance [8]. The transverse peak for  $\rho^+$  becomes very broad and is at  $M_\rho = 0.72$  GeV. The broadening of the transverse spectral density shows an accumulation of strength towards lower invariant mass region. There is no peak for  $\rho^-$  in the mass range considered, while for  $\rho^0$  it is at 0.4 GeV. This huge difference in the qualitative behaviour of the transverse and the longitudinal modes among the members of the triplet is clearly demonstrated at low propagation momentum of the  $\rho$  meson.

## 5 Summary

In summary, we have investigated the temperature and the density effects on the  $\rho$  meson spectral function with the effective Lagrangian in the chiral  $SU(3)$  model in isospin asymmetric nuclear medium. The spectral function of the  $\rho$  meson is studied by considering the effects of the decreasing neutron and proton effective masses within MFA. The inclusion of the neutron-proton asymmetry results in the modification of the pole position and the imaginary parts of the  $\rho$  meson self-energy in the medium, which in turn affects the spectral density of the particular particle concerned. Also this modification is different for different polarization states. The inclusion of the scalar-isovector field  $\delta$  which is responsible for the splitting of the neutron and the proton effective masses, in turn results in the splitting of the  $\rho$  meson triplet.

The properties of vector mesons in nuclear matter are studied in a varied range of density, temperature and asymmetry. Under the effects of the Fermi sea alone, one can see that the  $\rho^+$  takes a larger mass than  $\rho^0$  and  $\rho^-$ , with that of  $\rho^0$  lying in between. At finite temperature, the masses of  $\rho^+$  and  $\rho^0$  undergo an enhancement, while that of  $\rho^-$ , a reduction with increasing asymmetry.

The spectral densities of  $\rho$  meson propagating in asymmetric nuclear matter are evaluated in a mean free model. The meson spectral densities in matter are quite different from those in free space, the difference stemming due to a preferred frame attached to the nuclear matter. The transverse and the longitudinal components of the spectral density exhibit different qualitative behaviour in matter, whereas they are degenerate in free space. With increasing asymmetry, it can be seen that the splitting between the two modes of the triplet increases and this splitting is more pronounced for the transverse mode. While the peaks for  $\rho^+$  move to higher invariant mass regions, those for  $\rho^-$  move to lower invariant mass regions. The peak for  $\rho^0$  is almost around its nominal pole mass value. Moreover, for the same asymmetry and temperature, the splitting is found to increase when the density is increased. A large variation in the peak positions is observed when the propagation momentum of the  $\rho$  is small implying that the temperature/density effects are larger at small momentum.

The role of the magnetic interaction on the spectral properties is also analyzed by assuming running values for  $\kappa_{\rho NN}$ . The particles appear to be more stable when the vector coupling dominates over the tensor coupling within MFA. The splitting between the different modes is larger for a larger value of  $\kappa_{\rho NN}$  and the modification of the transverse component is larger. For large densities, within MFA the original distribution of the  $\rho$  changes completely, that it is no longer possible to interpret it as a particle.

This work can be extended to include arbitrary external magnetic fields to study the variation of the neutral and the charged  $\rho$  meson effective masses, their spectral functions and the dispersion relations with the external magnetic field.

The author gratefully acknowledges the financial support from the Department of Science & Technology, Government of India, for the project SR/WOS-A/PS/26/2013, Dr. Latha, Head of the Department of Physics, Providence Women's College, Calicut, for her support in carrying out this project at the Institute.

**Data Availability Statement** This manuscript has no associated data or the data will not be deposited. [Author's comment: The data generated during this particular study are all contained in this article.]

**Publisher's Note** The EPJ Publishers remain neutral with regard to jurisdictional claims in published maps and institutional affiliations.

## References

1. G.E. Brown, M. Rho, Phys. Rev. Lett. **66**, 2720 (1991).
2. T. Hatsuda, S.H. Lee, Phys. Rev. C **46**, R34 (1992).
3. G.Q. Li, C.M. Ko, G.E. Brown, Phys. Rev. Lett. **75**, 4007 (1995).
4. G. Chanfray, R. Rapp, J. Wambach, Phys. Rev. Lett. **76**, 368 (1996).
5. J.D. Walecka, Ann. Phys. (N.Y.) **83**, 491 (1974).
6. B.D. Serot, J.D. Walecka, Adv. Nucl. Phys. **16**, 1 (1986).
7. B.D. Serot, J.D. Walecka, Int. J. Mod. Phys. E **6**, 515 (1997).
8. C. Gale, J.I. Kapusta, Nucl. Phys. B **357**, 65 (1991).
9. S.A. Chin, Ann. Phys. **108**, 301 (1977).
10. H.-C. Jean, J. Piekarewicz, A.G. Williams, Phys. Rev. C **49**, 1981 (1994).
11. P.C. Rajee Bhageerathi, Int. J. Mod. Phys. E **21**, 1250063 (2012).
12. T.I. Gulamov, A.I. Titov, B. Kampfer, Phys. Lett. B **372**, 187 (1996).
13. Abhee K. Dutt-Mazumder, Nucl. Phys. A **611**, 442 (1996).
14. R. Aguirre, A.L. De Paoli, Eur. Phys. J. A **13**, 501 (2002).
15. Amruta Mishra, Arvind Kumar, arXiv:nucl-th/1003.0077.
16. S. Weinberg, Phys. Rev. **166**, 1568 (1968).
17. S. Coleman, J. Wess, B. Zumino, Phys. Rev. **177**, 2239 (1969).
18. C.G. Callan, S. Coleman, J. Wess, B. Zumino, Phys. Rev. **177**, 2247 (1969).
19. W.A. Bardeen, B.W. Lee, Phys. Rev. **177**, 2389 (1969).
20. P. Papazoglou, D. Zschesche, S. Schramm, J. Schaffner-Bielich, H. Stöcker, W. Greiner, Phys. Rev. C **59**, 411 (1999).
21. A. Mishra, K. Balazs, D. Zschesche, S. Schramm, H. Stöcker, W. Greiner, Phys. Rev. C **69**, 024903 (2004).
22. D. Zschesche, A. Mishra, S. Schramm, H. Stöcker, W. Greiner, Phys. Rev. C **70**, 045202 (2004).
23. J.J. Sakurai, *Currents and Mesons* (University of Chicago Press, Chicago, 1969).
24. A. Das, *Finite Temperature Field Theory* (World Scientific, Singapore, 1997).
25. M. Le Bellac, *Thermal Field Theory* (Cambridge University Press, 1996).
26. J.I. Kapusta, *Finite Temperature Field Theory* (Cambridge University Press, 1989).
27. C. Song, Phys. Rev. D **53**, 3962 (1996).
28. T. Hatsuda, H. Shiomi, H. Kuwabara, Prog. Theor. Phys. **95**, 1009 (1996).
29. R. Machleidt, K. Holinde, Ch. Elster, Phys. Rep. **149**, 1 (1987).
30. Octavian Teodorescu, Abhee K. Dutt-Mazumder, Charles Gale, Phys. Rev. C **66**, 015209 (2002).

# EVALUATION OF THE CYTOTOXICITY AND GENOTOXICITY OF RHIZOME EXTRACT OF HEDYCHIUM CORONARIUM USING THE ALLIUM TEST

<sup>1</sup>Pilty Peter A, <sup>2</sup>Jismine Mathew

<sup>1</sup>Assistant Professor on contract ,Providence Womens College, Calicut, Kerala, 673009,

<sup>2</sup>Providence College for teachers education, Calicut

## Abstract

Hedychium coronarium, the member of family of Zingiberaceae is a must-have plant in medicinal herb garden. It is reported that it contains phenols, terpenoids etc. The aim of this study was to evaluate the cytotoxic and genotoxic effects of rhizome extract of Hedychium coronarium on the *Allium cepa* cell cycle. Cells of root tips of *Allium cepa* were used as an *in vivo* test system for monitoring the genotoxicity of this medicinal plant. The slides were prepared by the squashing technique, scoring 12000 cells for each group of bulbs. The mitotic index (MI) was calculated and then a statistical analysis was performed using analysis of variance.. The results showed that rhizome extract caused a reduction of MI compared to control. The antiproliferative effect of rhizome extracts increased with a long duration . Mitotic anomalies keep on decreasing with increasing duration.

- **Keywords :** *Allium cepa* , *Hedychium coronarium*, Genotoxicity,

## Introduction

India is endowed with an enormous wealth of medicinal plants [12, 19] and is rightly called the “Medicinal Garden” of the world. The climatic diversity and regional topography of India accounts for the rich plant biodiversity [3]. India being one of the world’s top 12 mega diversity nations, harbours more than 8,000 medicinal plant species in its natural habitat. With the increasing acceptance of traditional medicine as an alternative form of health care the screening of medicinal plants for active compounds is very important traditional medicine based on plants has played a key role in the health care system of many countries like India,China etc., [16]. Herbal medicine is still the main stay of about 75-80% of the world population.

*Hedychium coronarium* is a genus commonly known as Ginger Lily originated in India and Indonesia. It is a top selling ginger and the most fragrant of all. Hedychium coronarium J. Koenig is a perennial medicinal herb which is distributed in throughout the world and used as traditional medicine since the ancient time. It contains various bioactive compounds including Phenols, Terpenoids, Saponins, Volatile oils, Flavonoids, Glycosides etc. These bioactive compounds made this herb as a valuable potent herbal drug. Hedychium

coronarium has high ethno medicinal significance in India and China as well.[13].It grows in Tropical rain forest near stream, canals or water channels. It is an annual or perennial aromatic herb with an underground rhizome with or without aerial stems. Rhizome is aromatic, fleshy, branched, and knotty, with many nodes and grows up to about 7.5 cm in diameter, spreading horizontally under the soil surface. Leaf is simple, alternate, radical or culine, usually distichous, with a sheathing petiole. Inflorescence erect, spike like, dense, ellipsoid, bracts persistent, imbricate, ovate, 4-5 by 2-4 cm, or 2-3 flowered per bract. Flowers hermaphrodite in racemes or spike, axillary or terminal, strongly zygomorphic, subtended by one or more bracts or spathes. Sepals 3, petals 3, united below in a tube. Androecium of 2 whorls of stamen and staminodes, only one stamen of the inner whorl is fertile, other 2 of the same whorl and all 3 of the outer whorl are modified into large petaloid staminodes, anther 2 locular. Ovary inferior, 3 celled, ovules many on axile placentation, style passing through the groove of fertile stamen, 2-lipped, and ovary rarely 1-celled with parietal or basal placentas. Seeds are many, with sticky red aril. It flowers between June-September [11]

Mitotic and replication indexes are used as indicators of adequate cell proliferation [8], which can be measured through the plant test system of *Allium cepa* L. [7], and the method of chromosome aberration in roots of *A. cepa* is validated by the International Program on Chemical Safety (IPCS, WHO) Pesticide residues in Food - Carbaryl . FAO Plant Production and Protection Paper - 140): <http://www.fao.org/docrep/W3727E/W3727E00.htm>,(1996) and the United Nations Environmental Programme (UNEP) as an efficient test for the analysis and monitoring *in situ* of the genotoxicity of environmental substances .

Accordingly, the cytotoxic and genotoxic effects of the rhizome extract of *Hedychium coronarium* was evaluated on the cell cycle and chromosomes of *Allium cepa* root meristems.

## MATERIALS AND METHODS

Fresh rhizome of *Hedychium coronarium* were collected, washed and extract was prepared by grinding the rhizome in pestle and motor. Fresh filtrates obtained were filtered using filter paper and used for every treatment. Fresh filtrates obtained were filtered using filter paper and used for every treatments. In this study, to evaluate the cytotoxic and genotoxic effects of the extracts of of *Hedychium coronarium* we applied the plant test system *Allium cepa*. the *A. cepa* test is considered an excellent bioindicator for the first screening of genotoxicity of medical plants, being a low cost test, reliable, and agreeing with other genotoxicity tests [2].Bioassay for monitoring the potential genotoxic effects of *Hedychium* extract was carried out according to the classical *Allium* test developed by[10]. commercially available onion was used as a test material. The dry outer rhizome were removed. The stem of the bulbs were scrapped slightly in

order to expose the root primordia. The bulbs were placed on 6 ml beakers containing distilled water. The basal plate of the onion bulb was held in contact with water and the water was changed every 24 hours to avoid contamination. After the emergence of roots about 3cm long were treated with the test compound for different durations at varying extracts. The durations of treatments ranged from 1hour, 2 and 4 hours. At the expiration of each of the treatment duration 4 – 6 roots were chopped from each treated bulb, including the control. They were washed 3 times in tap water and fixed in freshly prepared acetic ethanol (1:3). The fixed materials were stored in the refrigerator at least for 24 hours. Then they were washed thoroughly in distilled water and hydrolysed in 1N HCL in room temperature for 15mins. Then the roots were mordanted in 4 % ferric ammonium sulphate for 15 – 20 mins. And after washing in distilled water, they were stained in 0.5% haematoxylin for 10 – 12 mins. Haematoxylin was prepared by dissolving 0.5 gm of haematoxylin in 95% ethanol and finally the roots were washed and squashed in drop of 45% acetic acid on a clean slide and sealed with either DPX or Dunlop rubber solution. The prepared slides were examined under the microscope. Photomicrograms of the important stages of the interest were taken using Nikon microscope loaded with NOVA 125 ASA film. Various types of aberrations induced by each treatment at various stages were recorded. Analysis of variance was used to analyse the data obtained on the number of dividing cells at different mitotic phases and those with abnormalities.

### **Result And Discussion**

The present study was directed to determine the genotoxic effects of the test compound on biological systems. The allopathic medicines though superior, found to be causing side effects, and so comes the use of plant medicines. Though Hedygium has been suggested for many illness, there is no conclusive evidence supporting its use for any health conditions. Hence this study was designed to evaluate the genotoxic effects of Hedygium.

Measurement of chromosomal anomalies is an efficient, reliable and economic criterion to measure genotoxicity.[14] which could be indicated by alterations in structure and number. We see a significant reduction in Mitotic index during all durations of treatment.(Table1&Table2).However such adverse alterations were not so common in the control group. Hedygium had an immediate toxic effect on the dividing cells as it reduced the mitotic index after 1hr exposure. The reduction in the frequency of division showed a time dependent effect.

Hedygium also induced structural aberrations of chromosomes. Chromosomal anomalies like clumped, abortive,ringed,lagged chromosomes, multipolar anaphase, stickiness, anaphase and telophase bridges, and chromosomal clumps, were significantly higher when compared to the control samples. The number of aberrant cells were seemed to be decreased with increasing the duration of the treatment. The

Treatment of fresh rhizome extract of *Hedychium* for 1,2,4 hrs showed 59,62,51% of chromosomal anomalies. Some of the chromosomal anomalies were seen even in control samples.

The results of this study showed that rhizome extract of the studied *Hedychium coronarium* populations exhibit genotoxic effects, that is, they possess activity capable of inhibiting cell division.

*Hedychium coronarium* has tannins and flavonoids, among other chemicals in its chemical composition., Fachinetto *et al.* [7] found that *Achyroclin esatureidoides* (Lam) DC has antiproliferative activity on the *Allium cepa* cell cycle, Another example is the medicinal species *Pterocaulonn polystachyum* studied by Knoll *et al.* (2006), containing tannins and flavonoids in its chemical composition, and presenting antiproliferative activity on the *Allium cepa* cell cycle.

Cragg and Newman (2005) reported that many of the agents used in cancer therapy are derived from natural sources and were discovered from cytotoxicity tests, by inhibiting cancer cell proliferation in models *in vitro* or *ex vitro*. Therefore, it is of great importance to perform further studies on medicinal species that inhibit cell cycles, which is the case of *Hedychium coronarium* which demonstrates this capability especially with the high rate of mitotic inhibition on the *Allium cepa* cell cycle using the rhizome extract.

Sultan and Çelik (2009) investigated the genotoxic and antimutagenic extracts of the species *Capparis spinosa* L., because the aerial parts of this plant are widely used. The authors comment that in evaluating the effect of the complex mixture of the extracts of *C. spinosa* on *Allium cepa* cells, they found the aqueous extract not being genotoxic, though potentially antimutagenic.

*Hedychium* extract in this study have been shown to affect the mitotic apparatus and chromosome structure. These aberrations were termed mitoclassic and chromatoclassic effects, and respectively by Deysson (1968). According to Evandri *et al.* (2000) chromosome bridges and fragments are signs of clastogenic effects resulting from chromosome and chromatid breaks. The formation of bridges is attributed to several causes which includes

- i. Breaks that occur in both chromatids of the same chromosome and incorrect rejoining of the sticky ends to form a sister union. [1]
- ii. Incomplete replication of chromosomes by defective or less active replication enzymes [15] or through breaks that may occur late in the cell cycle after the chromosome have been replicated.

In this study, we can only indirectly assign the action of the chemical compounds present in both extracts of *Hedychium coronarium* used and tested with the *Allium cepa* test. However, we suggest that in future work the extraction of each of the products be carried out and analyzed. Although, in the case of aqueous extracts

(teas), we hypothesize that the predominant substances are responsible for the inhibitory action on cell division.

TABLE I

mitotic indices with the root meristems of allium cepa treated with fresh rhizome extract of hedechyum coronarium

Exp.No	Duration of treatment of hours	Total No. of cells scored	Total No. of cells in division	Mitotic index $n/N \times 100$	No. of cells in division			
					Prophase	Metaphase	Anaphase	Telophase
1	1hr	12507	800*	6.40*	330*	105*	104*	261*
2	2hrs	12472	505*	4.5*	213*	48*	41*	203*
3	4hrs	12454	340*	2.73*	219*	4*	7*	110*
4	Control	12245	985	8.04	428	135	134	288

\*The mean difference is significant

TABLE II

mitotic anomalies induced by fresh rhizome extract of hedychium coronarium in the root meristem of allium cepa

Exp. No	Duration of treatment of hours	Total No. of cells in division	No. of aberrant cells	Percentage of cells showing MAs	Types of Mitotic Anomalies														
					C	F	L	B	R	Br	TA	MA	DA	C-Met	Pul	MF	AA	PP	SA
1	1hr	800	477	59.63	98	6	22	31	16	37	6	1	72	63	-	6	119	-	-
2	2hrs	505	314	62.18	96	3	6	18	4	7	5	1	28	36	1	7	102	-	-
3	4hrs	340	176	51.76	79	-	-	7	-	8	-	-	10	20	5	8	39	-	-
4	Control*	985	19	1.93	-	7	-	2	-	-	-	2	-	-	-	-	8	-	-

\*Control grown in distilled water

C-clump, F-fragment, L-lag, B-break, R-ring, Br-bridge, TA-tripolar anaphase, MA -multipolar anaphase, DA-disturbed anaphase, C-Met-C-metaphase, Pul-pulverization, MF-multiple fragment, AA-aborted anaphase, PP-polyploidy, SA-star anaphase

## References

- [1]. Badr A. Ghareeb A, El-din HM., 1992, Cytotoxicity of some pesticides in mitotic cells of *Vicia faba* roots: Egypt. J. Appl. Sci, 7:457-468.
- [2]. Bagatini DB, da Silva ACF and Tedesco SB. 2007, *Uso do sistematizado de Allium cepa como indicador de genotoxicidade de infusões de plantas medicinais*: Revista Brasileira de Farmacognosia, 17(3): 4 .
- [3]. C.V.Chittibabu and N.Parthasarathy. 2000, Attenuated tree species diversity in human-impacted tropical Evergreen forest sites at Kolli Hills, Eastern Ghats, India: *Biodiversity and Conservation*. 9, pp.1493-1519.
- [4]. Cragg GM and Newman DJ. 2005, *Plants as a source of anti-cancer agents*: Journal of Ethnopharmacology, 100(1-2): 72-79.
- [5]. Deysson. 1968, 'Antibiotic substances' In: International Review of Cytology: 24:99-145, Bourne, G. Hand Danielli, J.F (eds), Academic Press Inc. New York. 24:99-145.
- [6]. Evandri MG, Tucci, P Bolle P. 2000, Toxicological evaluation of commercial mineral water bottled in polyethylene Terephthalate: a cytogenetic approach with *Allium cepa*. Food Addit. Contam, 17(1):1037-1045.
- [7]. Fachineto JM, Bagatini DB, Durigon J, da Silva ACF and Tedesco SB. 2007, *Efeito anti-proliferativo das infusões de Achyrocline satureioides DC (Asteraceae) sobre o ciclo celular de Allium cepa*: Revista Brasileira de Farmacognosia, 17(1): 49-54.
- [8]. Gadano A, Gurni A, López P, Ferraro G and Carballo M. 2002, *In vitro genotoxic evaluation of the medicinal plant Chenopodium ambrosioides L*: Journal of Ethnopharmacology, 81(1): 11-16.
- [9]. Knoll MF, da Silva ACF, do Canto-Dorow TS and Tedesco S B. 2006, *Effects of Pterocaulon polystachyum DC. (Asteraceae) on onion (Allium cepa) root-tip cells*: Genetics and Molecular Biology, 29(3): 539-542.
- [10]. Levan .1938, The effects of colchicines on root meristems in *Allium*: Hereditas, 24:471-486.
- [11]. Mukerjee, S. K. 1990, Family of Angiosperms : Monocotyledonae. In: College Botany. Vol. III, S. K. Mukerjee (eds): New Central Book Agency, Calcutta, 109-111.
- [12]. J. Maheswari. 2011, Patenting Indian medicinal plants and products: *Indian Journal of Science and Technology*: 4(3), pp. 298-301.
- [13]. Pooja Pachurekar, A. K. Dixit. 2017, Review Article A Review on Pharmacognostical Phytochemical and Ethnomedicinal Properties of *Hedychium coronarium* J. Koenig an Endangered Medicine: International Journal of Chinese Medicine: (2): 49-61.

[14]. Sharma A.K, Sharma A.1980,In chromosome technique :Theory and practice.Pub:Butterworth,London.

[15]. SinhaU.1979, Cytomorphological and macromolecular changes induced by P- fluorophenylalanine in *Allium cepa* and *triticale*.j: Cytol.Genet.,14:198.

[16]. Sudharsan, C.1998, Shoot bud regeneration from leaf explants of a medicinal plant *Enicostermaoxillare*: *Current science*:74:1099-1100.

[17]. Sultan, AO and Çelik, TA.2009, *Genotoxic and Antimutagenic Effects of Capparis spinosa L. on the Allium cepa L. Root Tip Meristem Cells*: *Caryologia*, 62(2):114-123.

[18]. Zeba Parveen and R.M.Shrivastava.2012, Biodiversity of India for global promotion of herbal medicine: a potent opportunity to boost the economy. *Indian Journal of Plant Sciences*.1 (2-3), pp. 137-143.

**FIRST AUTHOR- PILTY PETER A**

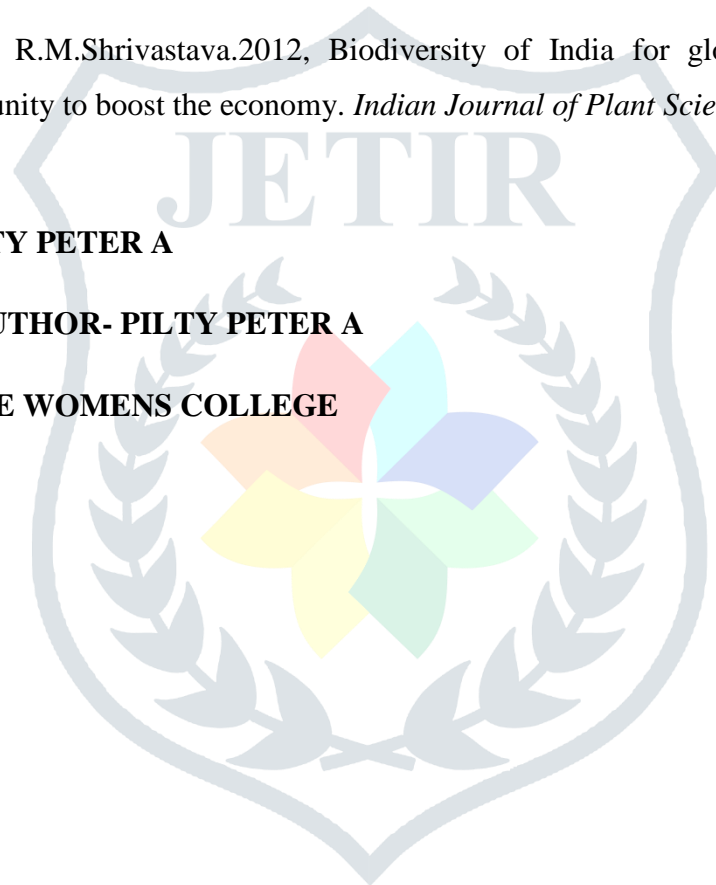
**CORRESPONDING AUTHOR- PILTY PETER A**

**Address- PROVIDENCE WOMENS COLLEGE**

**MALAPARAMBA P.O**

**CALICUT- 673009**

**KERALA**



# Establishing the spectral turnover of blazar PKS 2155–304 as an outcome of radiative losses

Sitha K. Jagan,<sup>1★</sup> S. Sahayanathan,<sup>2★</sup> R. Misra,<sup>3</sup> C. D. Ravikumar<sup>1</sup> and K. Jeena<sup>4</sup>

<sup>1</sup>*Department of Physics, University of Calicut, Malappuram 673635, India*

<sup>2</sup>*Astrophysical Sciences Division, Bhabha Atomic Research Centre, Mumbai 400085, India*

<sup>3</sup>*Inter-University Center for Astronomy and Astrophysics, Post Bag 4, Ganeshkhind, Pune 411007, India*

<sup>4</sup>*Department of Physics, Providence Women's College, Malaparamba, Calicut 673009, India*

Accepted 2018 May 7. Received 2018 May 4; in original form 2018 January 1

## ABSTRACT

The broad-band optical/UV and X-ray spectra of blazars have been often modelled as synchrotron component arising from a broken power-law distribution of electrons. A broken power-law distribution is expected, since the high-energy electrons undergo radiative losses effectively. The change in the energy index should then be  $\approx 1$  and corresponds to a spectral index difference of 0.5. However, one of the long outstanding problems has been that the observed index change is significantly different. On the other hand, recent high-quality observations of blazars suggest that their local spectra may not be a power law, instead have a slight curvature and often represented by a log-parabola model. Using *XMM-Newton* observations spanning over 12 yr for the BL Lac PKS 2155–304, we show that the optical/UV and X-ray spectra can be well represented by a broken log-parabola model. Further, we show that such a spectrum can indicate the energy dependence of the electron escape time-scale from the main acceleration zone. This novel approach, besides addressing the observed difference in the photon spectral indices, also tries to explain the spectral turn over in far-UV/soft X-rays as a result of the radiative losses.

**Key words:** acceleration of particles – diffusion – galaxies: active – BL Lacertae objects: individual: PKS 2155–304 – X-rays: galaxies.

## 1 INTRODUCTION

The low-energy synchrotron spectral component of blazars is reproduced by a broken power-law function suggesting the underlying electron distribution to be of broken power law in shape (Sambruna et al. 1994). A power-law electron distribution can be achieved under Fermi acceleration process, where the electrons gain energy while being scattered by magnetic turbulent structures embedded in the jet or by crossing a shock front (Rieger, Bosch-Ramon & Duffy 2007). Subsequently, the synchrotron losses modify the accelerated electron distribution into a broken power law with the indices differing by unity (Kardashev 1962; Heavens & Meisenheimer 1987). However, the observed difference between the low- and high-energy synchrotron spectral components of blazars cannot be perceived within the synchrotron cooling interpretation of a power-law electron distribution (Mankuzhiyil, Persic & Tavecchio 2010; Mankuzhiyil et al. 2012).

Around the peak of the synchrotron component, the blazar spectra deviate considerably from a power law with the spectra showing

smooth curvature. In many cases, the spectra at the peak are well reproduced by a log-parabola function suggesting the underlying electron distribution to be a log parabola as well (Massaro et al. 2004). The log-parabola function, however, is successful in explaining only a narrow-band of the spectrum falling around the peak but fails to explain the spectrum over a broad energy range, e.g. optical–X-ray energy bands (Massaro et al. 2004). Alternatively, the broad-band synchrotron component of blazars is often fitted with a smooth broken power-law function or a power law with an exponential cut off (Sinha et al. 2017).

PKS 2155–304 is a BL Lac class of blazars located at a redshift  $z = 0.116$ . Its synchrotron component peaks at UV energies (Madejski et al. 2016) and the broad-band spectrum reflects a smooth broken power-law function (Chiappetti et al. 1999; Aharonian et al. 2005). An extensive study of PKS 2155–304 was carried out by *XMM-Newton* at optical/UV (180–600 nm) and X-ray (0.15–12 keV) energy bands (Bhagwan et al. 2014; Gaur et al. 2017) on different epochs spanning more than a decade. The broad-band spectrum obtained through joint analysis of *NuSTAR* and *XMM-Newton* observations, supplemented with *Fermi* observations at gamma-ray energies, could be reproduced satisfactorily by a synchrotron and synchrotron self-Compton emission models due to a broken power-

\* E-mail: [sithajagan@gmail.com](mailto:sithajagan@gmail.com) (SJ); [sunder@barc.gov.in](mailto:sunder@barc.gov.in) (SS)

law electron distribution (Madejski et al. 2016). However, narrow-band X-ray analysis showed significant deviation from a power-law spectra (Gaur et al. 2017). Massaro et al. (2008) performed a detailed X-ray analysis of the source using *BeppoSAX*, *XMM-Newton*, and *Swift* observations from 1996 to 2007. They showed that the X-ray spectrum is well reproduced by a log-parabola function with the peak of the spectral energy distribution indicating a positive correlation with the spectral curvature. Nevertheless, the log-parabola model did not succeed well in explaining the combined optical/UV and the X-ray spectrum by *XMM-Newton* (Bhagwan et al. 2014).

In this work, we perform a detailed examination of *XMM-Newton* observations of PKS 2155–304 at optical/UV and X-ray energies. The optical/UV and X-ray data from 2000 November 19 to 2012 April 28 are analysed and the source spectra are obtained. The composite spectrum is then fitted with a broken log-parabola function. The rationale behind this being, the radiative cooling of a log-parabola electron distribution eventually modifies it into a broken log-parabola distribution. We also show that such an electron distribution can be achieved when the electron escape time-scale from the main acceleration region is energy dependent. Further, the analytical model developed under this scenario can fit the observed optical/UV and X-ray well and in turn, can hint the particle diffusion processes in active galactic nucleus jets.

## 2 OBSERVATIONS AND DATA REDUCTION

We selected 20 *XMM-Newton* archival data of PKS 2155–304, starting from 2000 November 19 to 2012 April 28, such that they have at least one simultaneous Optical/UV exposures with X-ray. For X-ray data, we used only the European Photon Imaging Camera (EPIC)-pn data and EPIC MOS data were avoided due to their low sensitivity, quantum efficiency, and chances of pile up. This data were reduced using *XMM-Newton* Science Analysis System (SAS Version 14.0) following standard procedures. The calibrated photon event files for the pn camera were produced using the command *epchain*. For pn data processing, both single and double events ( $PATTERN \leq 4$ ) of good quality ( $FLAG = 0$ ) in the energy range 0.2–10 keV were considered. In the 10–12 keV energy range, a ‘good time interval’ event list was produced by studying the light curve and fixing a threshold rate to omit background particle flaring.

The source spectrum was obtained using a circular region of size 40 arcsec around the source. The background was estimated using two circular regions of similar size located away from the source on the same source CCD chip. For nine observations, *epatplot* indicated significant pile-up and the source spectrum was extracted using an annular ring of inner radius 10 arcsec and an outer radius between 38 and 40 arcsec, within the CCD chip.

The optical monitor observations during the selected epochs were reprocessed with SAS pipeline *omichain*. The optical/UV data contain a significant galactic contamination which can manifest as large systematic error. To investigate this, we fitted the optical/UV data by a simple power-law function with addition of appropriate systematic error on data, required for better-fitting statistics. Four observations were discarded as they contained less than three optical/UV filter exposures. Similarly, two other observations demand a large systematic error ( $\gtrsim 30$  per cent) for a better statistics and hence they were also omitted in the present study. On an average, we found adding 3 per cent systematic error to the rest of 14 observations can result in better-fitting statistics. The details of these observations are given in Table 1.

## 3 BROKEN LOG-PARABOLA MODEL

The optical/UV and the X-ray data of PKS 2155–304 for the selected epochs were fitted with X-ray Spectral Fitting Package (XSPEC) using user-defined (local) and the inbuilt models (Arnaud 1996). The X-ray absorption due to Galactic neutral hydrogen in the direction of PKS 2155–304 was estimated by fixing the hydrogen column density to  $1.71 \times 10^{20} \text{ cm}^{-2}$  (Bhagwan et al. 2014). The optical/UV data were corrected for galactic reddening using the model UVRED by setting the parameter  $E_{B-V} = 0.019$  (Seaton 1979; Schlafly & Finkbeiner 2011). Similar to earlier works, the X-ray spectra were found to significantly deviate from a power-law and were better represented by a log parabola, but failed to explain the optical/UV data (Bhagwan et al. 2014; Gaur et al. 2017).

In order to develop a consistent model capable of fitting both the optical/UV and X-ray data, we considered a scenario where a log-parabola electron distribution is losing its energy under a synchrotron emission process (Massaro et al. 2004). For a small curvature, the radiative losses will steepen the index by  $\sim 1$  (Appendix). If the escape of electrons from the main emission region is also considered, then the electron distribution will transform into a broken log-parabola distribution with break occurring at an energy where the electron cooling time-scale is equal to the escape time-scale. The synchrotron spectrum resulting from such an electron distribution will again be a broken log parabola with the index differing by  $\approx 0.5$  (Sahayanathan, Sinha & Misra 2018).

To diagnose whether this interpretation is capable of explaining the broad-band distribution of PKS 2155–304, we performed a joint fitting of optical/UV and X-ray (0.6–10 keV) data using a broken log-parabola function defined by

$$F(\epsilon) \propto \begin{cases} \left(\frac{\epsilon}{\epsilon_b}\right)^{-\alpha+\Delta-\beta\log(\epsilon/\epsilon_b)}, & \text{for } \frac{\epsilon}{\epsilon_b} \leq 1 \\ \left(\frac{\epsilon}{\epsilon_b}\right)^{-\alpha-\beta\log(\epsilon/\epsilon_b)}, & \text{for } \frac{\epsilon}{\epsilon_b} > 1 \end{cases}. \quad (1)$$

Here  $\epsilon$  is the photon energy,  $\epsilon_b$  is the break energy,<sup>1</sup>  $\alpha$  is the index,  $\Delta$  is the difference between the indices, and  $\beta$  is the curvature parameter. Motivated by the synchrotron cooling interpretation of a log-parabola electron distribution, we fixed  $\Delta$  at 0.5 and obtained the best-fitting parameters. The fit results are given in Table 2. We also provide fit statistics, assuming a power-law model with a log-parabola tail following (Bhagwan et al. 2014), for comparison. In Fig. 1 (left) we show the spectral fit for the observation ID 0411780501. The best-fitting X-ray, UV, and optical fluxes are also given in Table 1. The X-ray spectra corresponding to the observation IDs 0158961401, 0411780101, and 0411780201 show significant negative curvature suggesting a plausible contribution of Compton spectral component. Hence, for these observations the model parameters cannot be constrained effectively. Presence of Compton contamination was evident in most of the observations with the high-energy data deviating considerably from the best-fitting model (Fig. 1).

A Spearman rank correlation analysis between the flux and the fitted parameters was performed to investigate their dependence. We found no significant correlation between these quantities. However, a weak negative correlation between the curvature parameter  $\beta$  and the optical/UV flux can be seen with the lowest null hypothesis probability  $P_{\text{ns}} = 0.03$  and corresponding rank correlation coefficient  $r_s = -0.62$ . This correlation is not very significant and

<sup>1</sup> Here  $\epsilon_b$  is the energy at which the two log-parabola functions assume the same value and not the peak of the log parabola.

**Table 1.** Observation details of PKS 2155–304 with *XMM–Newton* and the best-fitting X-ray and optical/UV fluxes. Pile-up was noticed for the observation IDs with \*.

Obs. ID	Exposure (s)	Flux ( $10^{-11} \text{ erg cm}^{-2} \text{ s}^{-1}$ )						
		X-ray	UVW2	UVM2	UVW1	U	B	V
0124930501*	104 868	$7.534^{+0.036}_{-0.037}$	$0.782^{+0.039}_{-0.039}$	–	–	$2.171^{+0.110}_{-0.111}$	$1.004^{+0.051}_{-0.051}$	$4.419^{+0.291}_{-0.278}$
0124930601	114 675	$5.161^{+0.013}_{-0.012}$	$0.733^{+0.036}_{-0.037}$	$1.844^{+0.092}_{-0.092}$	$1.256^{+0.062}_{-0.063}$	$1.989^{+0.101}_{-0.099}$	$0.955^{+0.048}_{-0.048}$	$3.607^{+0.198}_{-0.194}$
0158960101	27 159	$4.492^{+0.017}_{-0.018}$	–	$2.68^{+0.136}_{-0.135}$	$1.841^{+0.091}_{-0.092}$	$2.909^{+0.148}_{-0.148}$	–	–
0158960901	28 919	$4.849^{+0.0162}_{-0.0162}$	–	–	–	$2.981^{+0.152}_{-0.149}$	$1.38^{+0.070}_{-0.069}$	$5.674^{+0.349}_{-0.337}$
0158961001	40 419	$6.714^{+0.017}_{-0.017}$	$1.05^{+0.052}_{-0.052}$	$2.599^{+0.129}_{-0.130}$	$1.851^{+0.092}_{-0.092}$	–	$1.341^{+0.067}_{-0.067}$	–
0158961301*	60 415	$10.617^{+0.033}_{-0.033}$	$2.032^{+0.102}_{-0.101}$	$5.603^{+0.280}_{-0.281}$	$3.778^{+0.187}_{-0.188}$	$5.989^{+0.303}_{-0.302}$	$2.86^{+0.144}_{-0.144}$	$14.695^{+0.906}_{-0.880}$
0158961401*	64 814	$4.506^{+0.023}_{-0.022}$	$1.277^{+0.064}_{-0.064}$	$3.561^{+0.180}_{-0.179}$	$2.622^{+0.131}_{-0.129}$	$4.299^{+0.221}_{-0.218}$	$2.12^{+0.108}_{-0.108}$	$10.729^{+0.722}_{-0.687}$
0411780101	101 012	$6.02^{+0.015}_{-0.022}$	$1.855^{+0.093}_{-0.092}$	$5.012^{+0.248}_{-0.249}$	$3.394^{+0.167}_{-0.168}$	$5.652^{+0.279}_{-0.280}$	$2.749^{+0.136}_{-0.136}$	$14.685^{+0.738}_{-0.747}$
0411780201*	67 911	$13.178^{+0.036}_{-0.035}$	$2.143^{+0.107}_{-0.107}$	$5.715^{+0.284}_{-0.285}$	$4.049^{+0.201}_{-0.199}$	$6.872^{+0.342}_{-0.344}$	$3.123^{+0.156}_{-0.155}$	$15.842^{+0.887}_{-0.871}$
0411780301*	61 216	$16.125^{+0.042}_{-0.043}$	$1.588^{+0.079}_{-0.079}$	$4.104^{+0.205}_{-0.205}$	$2.793^{+0.138}_{-0.139}$	$4.138^{+0.206}_{-0.207}$	$1.947^{+0.098}_{-0.097}$	$7.901^{+0.426}_{-0.418}$
0411780401*	64 820	$8.811^{+0.024}_{-0.025}$	$1.739^{+0.087}_{-0.087}$	$4.589^{+0.229}_{-0.229}$	$3.181^{+0.158}_{-0.157}$	$5.162^{+0.259}_{-0.259}$	$2.377^{+0.119}_{-0.119}$	$10.209^{+0.588}_{-0.577}$
0411780501	74 298	$5.254^{+0.019}_{-0.019}$	$0.959^{+0.048}_{-0.049}$	$2.461^{+0.124}_{-0.124}$	$1.642^{+0.081}_{-0.082}$	$2.493^{+0.128}_{-0.128}$	$1.182^{+0.061}_{-0.059}$	$5.109^{+0.315}_{-0.301}$
0411780601*	63 818	$7.523^{+0.026}_{-0.026}$	$1.022^{+0.053}_{-0.050}$	$2.545^{+0.127}_{-0.128}$	$1.792^{+0.089}_{-0.089}$	$2.844^{+0.143}_{-0.143}$	$1.354^{+0.068}_{-0.068}$	$5.551^{+0.318}_{-0.310}$
0411780701	68 735	$1.466^{+0.007}_{-0.007}$	$0.452^{+0.023}_{-0.024}$	$1.254^{+0.064}_{-0.064}$	$0.841^{+0.042}_{-0.042}$	$1.369^{+0.071}_{-0.070}$	$0.668^{+0.035}_{-0.034}$	$3.414^{+0.238}_{-0.199}$

**Table 2.** Fit results of optical/UV and X-ray spectrum using broken log-parabola model and the synchrotron emission with energy dependent electron escape from the main acceleration region. In column 6 we provide the fit statistics for a power-law + log-parabola model (PLL) following et al. (2014) for comparison and the fit parameters are similar to the values reported.

Obs. ID	Broken log parabola				PLL		Energy dependent escape		
	$\alpha$	$\beta$	$\epsilon_b$	$\chi^2/\text{d.o.f.}$	$\chi^2/\text{d.o.f.}$	$\psi$	$\beta'$	$\epsilon'_b$	$\chi^2/\text{d.o.f.}$
0124930501	$2.49^{+0.05}_{-0.03}$	$0.083^{+0.012}_{-0.011}$	$0.15^{+0.07}_{-0.05}$	199.6/167	324.14/167	$16.06^{+4.60}_{-2.69}$	$0.12^{+0.02}_{-0.02}$	$0.13^{+0.07}_{-0.04}$	200.69/167
0124930601	$2.35^{+0.04}_{-0.09}$	$0.137^{+0.011}_{-0.004}$	$0.05^{+0.01}_{-0.02}$	302.7/204	300.41/204	$8.03^{+1.03}_{-0.90}$	$0.21^{+0.02}_{-0.02}$	$0.04^{+0.01}_{-0.01}$	282.26/204
0158960101	$2.78^{+0.04}_{-0.06}$	$0.071^{+0.010}_{-0.010}$	$0.39^{+0.21}_{-0.15}$	191.9/166	355.02/166	$31.29^{+10.12}_{-8.62}$	$0.08^{+0.03}_{-0.02}$	$0.39^{+0.21}_{-0.17}$	191.70/166
0158960901	$2.72^{+0.05}_{-0.15}$	$0.135^{+0.020}_{-0.011}$	$0.21^{+0.12}_{-0.11}$	176.6/167	278.26/167	$14.65^{+3.23}_{-2.57}$	$0.17^{+0.02}_{-0.02}$	$0.19^{+0.12}_{-0.07}$	179.76/167
0158961001	$2.45^{+0.08}_{-0.07}$	$0.148^{+0.008}_{-0.011}$	$0.07^{+0.03}_{-0.02}$	285.0/193	396.31/193	$10.05^{+1.66}_{-1.05}$	$0.20^{+0.01}_{-0.02}$	$0.08^{+0.03}_{-0.01}$	287.91/193
0158961301	$2.48^{+0.03}_{-0.06}$	$0.073^{+0.011}_{-0.006}$	$0.07^{+0.02}_{-0.02}$	293.8/196	480.18/196	$18.27^{+3.75}_{-2.72}$	$0.11^{+0.01}_{-0.02}$	$0.06^{+0.02}_{-0.01}$	293.70/196
0411780301	$2.33^{+0.06}_{-0.04}$	$0.105^{+0.005}_{-0.010}$	$0.06^{+0.02}_{-0.01}$	233.6/209	382.12/209	$10.99^{+1.62}_{-1.37}$	$0.16^{+0.01}_{-0.01}$	$0.06^{+0.02}_{-0.01}$	234.47/209
0411780401	$2.60^{+0.07}_{-0.04}$	$0.114^{+0.006}_{-0.016}$	$0.13^{+0.07}_{-0.02}$	275.9/200	500.10/200	$15.86^{+2.21}_{-1.97}$	$0.14^{+0.01}_{-0.01}$	$0.13^{+0.04}_{-0.03}$	283.91/200
0411780501	$2.47^{+0.06}_{-0.07}$	$0.123^{+0.011}_{-0.009}$	$0.07^{+0.03}_{-0.02}$	217.5/174	327.97/174	$11.76^{+1.87}_{-1.63}$	$0.17^{+0.02}_{-0.02}$	$0.07^{+0.02}_{-0.02}$	225.30/174
0411780601	$2.29^{+0.06}_{-0.05}$	$0.080^{+0.008}_{-0.009}$	$0.03^{+0.01}_{-0.01}$	231.0/195	261.58/195	$12.40^{+2.62}_{-2.06}$	$0.13^{+0.02}_{-0.02}$	$0.03^{+0.01}_{-0.01}$	229.30/195
0411780701	$2.66^{+0.06}_{-0.06}$	$0.105^{+0.010}_{-0.011}$	$0.12^{+0.05}_{-0.03}$	233.8/154	361.85/154	$18.45^{+3.40}_{-2.80}$	$0.13^{+0.02}_{-0.02}$	$0.12^{+0.05}_{-0.03}$	239.36/154

hence we speculate that the spectral shape does not have any implication on the observed flux level rather may depend on dynamics which are unrelated to the flux variation. A plausible scenario can be the spectral curvature being dependent on the electron diffusive processes which may not have a direct association with the flux variation.

#### 4 ELECTRON ESCAPE TIME-SCALE AND SPECTRAL CURVATURE

To interpret the spectral curvature and the broken log-parabola representation of the observed optical/UV and X-ray spectra of PKS 2155–304, we considered a scenario where the electrons are accelerated at a shock front and escape into the downstream region where they lose their energy through radiative processes. Consistently, we label the region around the shock front as acceleration

region (AR) and the downstream region as emission region (ER). In general, the steady state non-thermal electron distribution  $n(\gamma)$  generated by an acceleration process which is balanced by the escape rate can be expressed as (e.g. Kardashev 1962)

$$\frac{d}{d\gamma} \left[ \left( \frac{\gamma}{\tau_a} - \zeta \gamma^2 \right) n(\gamma) \right] + \frac{n(\gamma)}{\tau_e} = Q_0 \delta(\gamma - \gamma_0). \quad (2)$$

Here we assume a mono energetic injection into AR at energy  $\gamma_0$ ,  $\gamma$  being the dimensionless electron energy and,  $\tau_a$  and  $\tau_e$  define the characteristic acceleration and escape time-scales, respectively. The radiative loss rate encountered by the electrons in AR is determined by  $\zeta \gamma^2$ . Expressing  $\zeta$  in terms of maximum Lorentz factor  $\gamma_{\max}$  attained by the electron,  $\zeta = (\gamma_{\max} \tau_a)^{-1}$ , equation (2) can be reduced, for  $\gamma_0 < \gamma \ll \gamma_{\max}$ , to

$$\frac{d}{d\gamma} \left[ \frac{\gamma}{\tau_a} n(\gamma) \right] = -\frac{n(\gamma)}{\tau_e}. \quad (3)$$

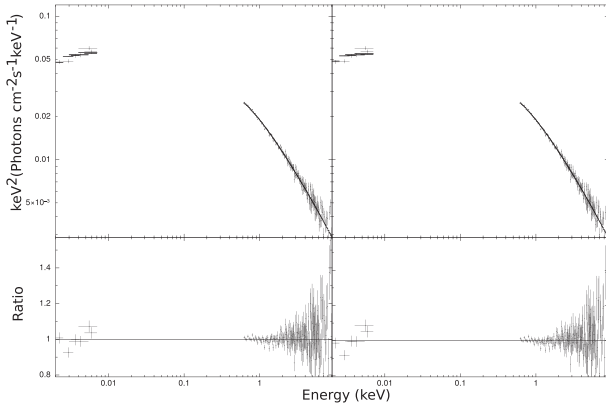


**Figure 1.** Unfolded optical/UV and X-ray spectrum along with best-fitting models for Observation ID 0411780501. The models are broken log-parabola (left) and synchrotron emission with energy dependent electron escape (right).

This can be rewritten for an energy independent  $\tau_a$  as

$$\frac{d \ln S(\gamma)}{d \ln \gamma} = -\xi, \quad (4)$$

where  $S(\gamma) = \gamma n(\gamma)$  is the energy density and  $\xi = \tau_a / \tau_e$ . If we assume  $\tau_e$  also to be energy independent, then the resulting electron distribution will be a power law  $n(\gamma) \propto \gamma^{-p}$  with index  $p = \xi + 1$ . On the other hand, if we consider the escape time-scale to be energy dependent such that  $\xi$  takes a form  $\xi = \xi_0 \gamma^{\beta'}$ , then equation (4) will have a solution

$$S(\gamma) \propto \exp\left(-\frac{\xi_0}{\beta'} \gamma^{\beta'}\right). \quad (5)$$

Similarly, the steady state non-thermal electron distribution  $N(\gamma)$  in ER can be expressed as

$$-\frac{d}{d\gamma} [\eta \gamma^2 N(\gamma)] + \frac{N(\gamma)}{t_e} = \frac{n(\gamma)}{\tau_e(\gamma)}, \quad (6)$$

where  $\eta \gamma^2$  is the radiative loss rate in ER and  $t_e$  is the characteristic escape time-scale from ER. For energy independent  $t_e$ , solution to equation (6) will be of the form

$$N(\gamma) \propto \begin{cases} \gamma^{\beta'-1} \exp\left(-\frac{\xi_0}{\beta'} \gamma^{\beta'}\right), & \text{for } \gamma \ll \gamma_b \\ \gamma^{-2} \exp\left(-\frac{\xi_0}{\beta'} \gamma^{\beta'}\right), & \text{for } \gamma \gg \gamma_b \end{cases}, \quad (7)$$

where  $\gamma_b$  corresponds to the energy for which the cooling time-scale equals to  $t_e$ . The synchrotron photon flux due to this electron distribution will be (Sahayanathan et al. 2018)

$$F_{\text{syn}}(\epsilon) \propto \begin{cases} \epsilon^{-1+\beta'/2} \exp(-\psi \epsilon^{\beta'/2}), & \text{for } \frac{\epsilon}{\epsilon_b} \ll 1 \\ \epsilon^{-3/2} \exp(-\psi \epsilon^{\beta'/2}), & \text{for } \frac{\epsilon}{\epsilon_b} \gg 1 \end{cases}, \quad (8)$$

where  $\psi$  is a parameter relating the observed photon frequency with electron energy and  $\epsilon_b$  is the emitted photon energy corresponding to electron energy  $\gamma_b$ . For  $\beta' \ll 1$ , equation (8) will be equivalent to equation (1) with the parameters related as

$$\beta' \approx \frac{3.5 \beta}{2\alpha - 3}, \quad \psi \approx \frac{(2\alpha - 3)^2}{3.5 \beta}. \quad (9)$$

The observed optical/UV and X-ray data of PKS 2155–304 for the selected epochs were fitted using the synchrotron spectrum from ER given by (8). Similar to the broken log-parabola function, we found that this physical model can also fit observations well and

in Table 2, we provide the fit results. In Fig. 1 (right) we show the spectral fit corresponding to this model for the observation ID 0411780501. This study, thereby, suggests the observed curvature in the X-ray spectrum of blazars may indicate energy dependence of the escape time-scale. This in turn will depend on the electron diffusion in the jet medium and hence can provide information regarding the magnetic field structure of blazar jets.

## 5 DISCUSSION

We show that the combined optical/UV and X-ray observations of PKS 2155–304 using *XMM-Newton*, spanning over a period of 12 yr, are better represented by a broken log-parabola function with minimal curvature. The index differences are consistent with the spectral turnover introduced by synchrotron loss of a parent log-parabola electron distribution. This study, thereby, resolves the inadequacy of the broken power-law representation of blazar spectra to explain the index difference under the synchrotron loss phenomena. Further, we show that the curvature of the fitted function can indicate the energy dependence of the electron escape rate from the main acceleration region. The simplistic physical model developed under this scenario can fit the observed optical/UV and X-ray data very well.

The spectral and temporal properties of PKS 2155–304 were also studied by Kapanadze et al. (2014) using *Swift* observations during 2005–2012. The X-ray spectra showed significant curvature and were reproduced better by a log-parabola function. The observed anticorrelation between the spectral index at 1 and 0.3–10 keV flux suggested that the spectra harden at high-flux states. The non-availability of information at low energy prevents the authors from precise estimation of the peak energy. A log-parabola X-ray spectral shape of PKS 2155–304 was already identified in *XMM-Newton* observations during a period overlapping with the one considered here (Gaur et al. 2017). However, the main attempt of these works was to highlight the curved X-ray spectra and their behaviour during different flux states. On the other hand, here we perform a joint spectral fitting of optical–X-ray spectra. The inadequacy of a log-parabola function to explain the combined optical–X-ray spectra was initially shown by Massaro et al. (2004), for the case of MKN 421. In case of PKS 2155–304, a satisfactory fit of optical–X-ray spectra can be obtained by PLLP model (Bhagwan et al. 2014). A plausible scenario under which such a spectrum can be obtained is when the electron escape time-scale in ER is energy dependent; whereas, the acceleration and escape time-scales in AR are energy independent (Sinha et al. 2017). The resultant particle distribution in AR will then be a power law. On subsequent injection into ER, it will develop a smooth curvature at high energy, imitating a log parabola. On the other hand, here we show that a broken log parabola can provide a better fit without invoking additional number of parameters. This asserts the energy dependence of the escape time-scale in AR rather than the ER.

Through this work, we demonstrate that the slight curvature observed in addition to the power-law component in the blazar spectra can be translated into energy dependence of the escape time-scale from the main acceleration region. This identification, in turn, can provide clues on the electron diffusion processes in blazar jets. For instance, if the electron diffusion is mainly governed through pitch angle scattering, then this result can be helpful in understanding the magneto hydrodynamic nature of the blazar jets (Summerlin & Baring 2012). Alternatively, the information about the energy dependence of the escape time-scale can indicate the magnetic field alignment in blazar emission zone (Achterberg & Ball 1994). This

energy dependence can be coupled with cross-field and/or align-field diffusion coefficients and supplemented with the polarization information; this can be used to draw a global picture regarding the magnetic field structure in blazars.

## ACKNOWLEDGEMENTS

This research is based on the observations obtained with *XMM-Newton* satellite, an ESA science mission with instruments and contributions directly funded by ESA member states and NASA. This work has made use of the NASA/IPAC Extra Galactic Database operated by Jet Propulsion Laboratory, California Institute of Technology and the High Energy Astrophysics Science Archive Research Center (HEASARC) provided by NASA's Goddard Space Flight Center. SKJ thanks Jithesh V. and Savithri H. Ezhikode for useful discussions. SKJ thanks the University Grants Commission for the financial support through the Rajiv Gandhi National Fellowship scheme. Authors thank the anonymous referee for the comments that improved the quality of the manuscript.

## REFERENCES

- Achterberg A., Ball L., 1994, *A&A*, 285, 687  
 Aharonian F. et al., 2005, *A&A*, 442, 895  
 Arnaud K. A., 1996, in Jacoby G. H., Barnes J., eds, ASP Conf. Ser. Vol. 101, *Astronomical Data Analysis Software and Systems V*. Astron. Soc. Pac., San Francisco, p. 17  
 Bhagwan J., Gupta A. C., Papadakis I. E., Wiita P. J., 2014, *MNRAS*, 444, 3647  
 Chiappetti L. et al., 1999, *ApJ*, 521, 552  
 Gaur H., Chen L., Misra R., Sahayanathan S., Gu M. F., Kushwaha P., Dewangan G. C., 2017, *ApJ*, 850, 209  
 Heavens A. F., Meisenheimer K., 1987, *MNRAS*, 225, 335  
 Kapanadze B., Romano P., Vercellone S., Kapanadze S., 2014, *MNRAS*, 444, 1077  
 Kardashev N. S., 1962, *SvA*, 6, 317  
 Madejski G. M. et al., 2016, *ApJ*, 831, 142  
 Mankuzhiyil N., Persic M., Tavecchio F., 2010, *ApJ*, 715, L16  
 Mankuzhiyil N., Ansoldi S., Persic M., Rivers E., Rothschild R., Tavecchio F., 2012, *ApJ*, 753, 154  
 Massaro E., Perri M., Giommi P., Nesci R., 2004, *A&A*, 413, 489  
 Massaro F., Tramacere A., Cavaliere A., Perri M., Giommi P., 2008, *A&A*, 478, 395  
 Rieger F. M., Bosch-Ramon V., Duffy P., 2007, *Ap&SS*, 309, 119  
 Sahayanathan S., Sinha A., Misra R., 2018, *RAA*, 18, 35  
 Sambruna R. M., Barr P., Giommi P., Maraschi L., Tagliaferri G., Treves A., 1994, *ApJS*, 95, 371
- Schlafly E. F., Finkbeiner D. P., 2011, *ApJ*, 737, 103  
 Seaton M. J., 1979, *MNRAS*, 187, 73P  
 Sinha A., Sahayanathan S., Acharya B. S., Anupama G. C., Chitnis V. R., Singh B. B., 2017, *ApJ*, 836, 83  
 Summerlin E. J., Baring M. G., 2012, *ApJ*, 745, 63

## APPENDIX: LOG-PARABOLA ELECTRON DISTRIBUTION UNDERGOING RADIATIVE LOSSES

A log-parabola electron distribution,  $u(\gamma)$ , undergoing synchrotron loss can be described by

$$-\frac{d}{d\gamma} [\zeta \gamma^2 u(\gamma)] = Q_0 \gamma^{-a-b \ln \gamma}. \quad (\text{A1})$$

Here  $\zeta \gamma^2$  is the radiative energy loss rate. Equation (A1) can be rewritten as

$$\frac{d \ln W(\gamma)}{d \ln \gamma} = -\frac{Q_0}{\zeta W(\gamma)} \gamma^{-a+1-b \ln \gamma}, \quad (\text{A2})$$

where  $W(\gamma) = \gamma^2 u(\gamma)$ . We assume a priori that the solution  $W(\gamma)$  is of a log-parabola type:

$$W(\gamma) = W_0 \gamma^{-c-d \ln \gamma} \quad (\text{A3})$$

and recast equation (A2) to

$$\frac{d \ln W(\gamma)}{d \ln \gamma} = -\frac{Q_0}{\zeta W_0} \gamma^\kappa \approx -\frac{Q_0}{\zeta W_0} (1 + \kappa \ln \gamma), \quad (\text{A4})$$

where  $\kappa = -a + c + 1 - (b - d) \ln \gamma \ll 1$ . Using equation (A3)

$$\frac{d \ln W(\gamma)}{d \ln \gamma} = -c - 2d \ln \gamma. \quad (\text{A5})$$

Comparing equations (A4) and (A5), we note that for consistency  $\kappa$  is required to be energy independent and hence,  $d = b$ . Moreover,  $c(c - a + 1) = 2b$  and for  $b \ll 1$ ,

$$c \approx (a - 1) \left[ 1 + \frac{2b}{(a - 1)^2} \right].$$

The resultant electron distribution will be,

$$u(\gamma) \propto \gamma^{-(a+1)-b \ln \gamma - \frac{2b}{a-1}}. \quad (\text{A6})$$

Hence, the synchrotron loss process steepens the injected log-parabola distribution by  $1 + \frac{2b}{a-1}$ .

This paper has been typeset from a  $\text{\TeX}/\text{\LaTeX}$  file prepared by the author.